Molecular Therapy
Nucleic Acids
Original Article

Enhancing peptide and PMO delivery to mouse airway epithelia by chemical conjugation with the amphiphilic peptide S10

Maud Auger,[1,3,4] Luis Sorroza-Martinez,[1,3,4] Nadine Brahiti,[1,4] Carole-Ann Huppé,[2] Laurence Faucher-Giguère,[1] Imen Arbi,[1] Maxime Hervault,[1] Xue Cheng,[1] Bruno Gaillet,[3] Frédéric Couture,[2] David Guay,[1,3] and Al-Halifa Soultan[1]

[1]Feldan Therapeutics, 2666 Boulevard du Parc Technologique Suite 290, Québec, QC G1P 4S6, Canada; [2]Centre Collégial de Transfert de Technologie en Biotechnologies TransBIOTech, 201 Rue Monseigneur-Bourget, Lévis, QC G6V 6Z3, Canada; [3]Département de génie chimique, Faculté des Sciences et de Génie, Université Laval, Pavillon Adrien-Pouliot 1065, av. de la Médecine, Bureau 3550, Québec, QC G1V 0A6, Canada

Delivery of antisense oligonucleotides (ASOs) to airway epithelial cells is arduous due to the physiological barriers that protect the lungs and the endosomal entrapment phenomenon, which prevents ASOs from reaching their intracellular targets. Various delivery strategies involving peptide-, lipid-, and polymer-based carriers are being investigated, yet the challenge remains. S10 is a peptide-based delivery agent that enables the intracellular delivery of biomolecules such as GFP, CRISPR-associated nuclease ribonucleoprotein (RNP), base editor RNP, and a fluorescent peptide into lung cells after intranasal or intratracheal administrations to mice, ferrets, and rhesus monkeys. Herein, we demonstrate that covalently attaching S10 to a fluorescently labeled peptide or a functional splice-switching phosphorodiamidate morpholino oligomer improves their intracellular delivery to airway epithelia in mice after a single intranasal instillation. Data reveal a homogeneous delivery from the trachea to the distal region of the lungs, specifically into the cells lining the airway. Quantitative measurements further highlight that conjugation via a disulfide bond through a pegylated (PEG) linker was the most beneficial strategy compared with direct conjugation (without the PEG linker) or conjugation via a permanent thiol-maleimide bond. We believe that S10-based conjugation provides a great strategy to achieve intracellular delivery of peptides and ASOs with therapeutic properties in lungs.

INTRODUCTION

Delivery of therapeutic biomolecules such as antisense oligonucleotides (ASOs), peptides, and proteins to the lung is challenging because of the physical and cellular barriers formed by the airway epithelia, the host defense mechanisms such as secretion factors, and the mucociliary clearance.[1–3] Among the various inhaled biomolecules investigated to treat lung diseases, ASOs are attractive due to their ability to mediate RNA degradation, alternative splicing, or suppress translation of targeted RNA sequences without affecting genomic DNA.[4,5] Several ASOs have shown promising results for the treatment of respiratory diseases such as asthma and cystic fibrosis (CF).[6–11] Among the different ASO derivatives, phosphorodiamidate morpholino oligomers (PMOs) have great potential as therapeutic biomolecules. PMOs are ASOs in which the phosphodiester is replaced by a phosphorodiamidate backbone and the ribose by a morpholino subunit. These structural modifications grant PMOs attractive features such as strong nuclease resistance and neutral net charge, leading to high metabolic stability and low detection by the immune system *in vivo*.[12–14] With such properties, PMOs have been successfully approved by the US Food and Drug Administration (FDA) to restore dystrophin protein expression in muscles of Duchenne muscular dystrophy (DMD) patients after systemic administration.[15–19] Nevertheless, except in the case of altered tissues such as deteriorated muscle membranes in DMD,[20,21] *in vitro* and *in vivo* studies show that PMOs are internalized into cells but remain mostly trapped in endosomes, which prevents them from reaching intracellular RNA molecules.[22,23]

Several strategies have been developed to improve ASO delivery, including polymer- or lipid-based nanoparticles and ligand conjugation.[24–31] However, these approaches have yet to be validated with clinical data in the context of lung delivery. Regarding PMOs, one interesting approach consists of covalently attaching the PMO to a cationic peptide, such as cell-penetrating peptides (CPPs), known for their ability to improve cellular uptake.[26–29] However, despite enhancing cell entry, CPP-conjugated PMOs (CPP-PMO), also known as peptide-morpholino oligomer conjugates (PPMOs), still

Received 16 January 2024; accepted 26 July 2024;
https://doi.org/10.1016/j.omtn.2024.102290.

[4]These authors contributed equally

Correspondence: David Guay, Feldan Therapeutics, 2666 Boulevard du Parc Technologique Suite 290, Québec, QC G1P 4S6, Canada.
E-mail: dguay@feldan.com
Correspondence: Al-Halifa Soultan, Feldan Therapeutics, 2666 Boulevard du Parc Technologique Suite 290, Québec, QC G1P 4S6, Canada.
E-mail: ahsoultan@feldan.com

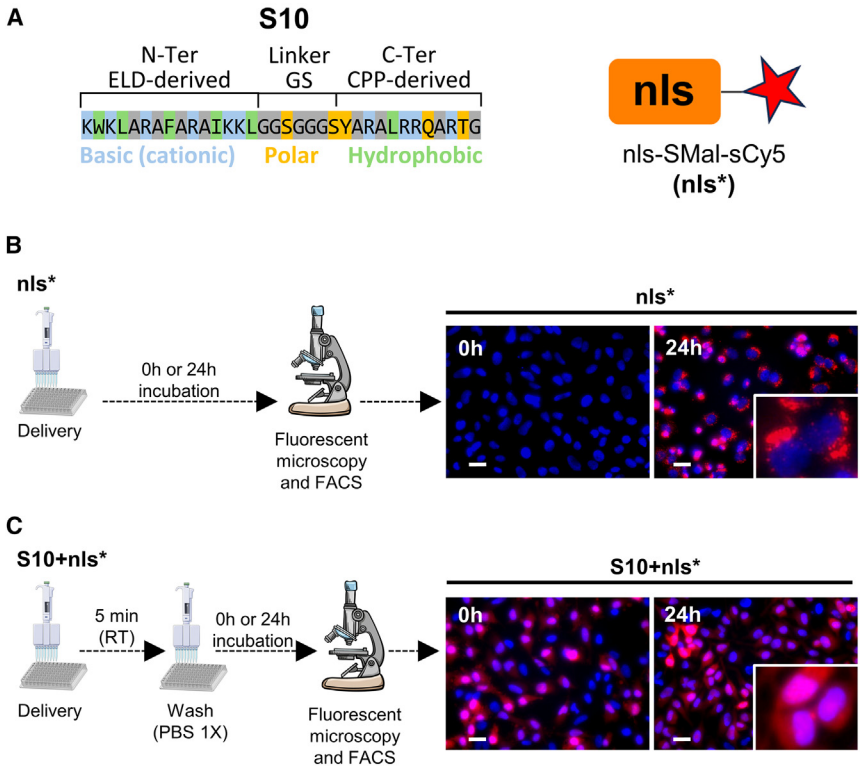

Figure 1. Cellular uptake in wild-type HeLa cells of nls* and the mixture S10+nls*

(A) Structure of S10 (left) and **nls*** (right). (B) Schematic of the delivery and cellular uptake of **nls*** by live imaging microscopy. (C) Schematic of the delivery experiments for the **S10+nls*** mixture and its intracellular delivery by live imaging microscopy. Live imaging was performed on a Revolve R4 hybrid inverted fluorescence microscope at 20× magnification (scale bars, 30 μm). Hoechst 33342 (blue) shows cell nuclei and Cy5 (red) is the fluorescent dye in compound **nls***.

struggle to escape endosomal entrapment.[23] To specifically address this issue, co-administration of PPMOs with oligonucleotide-enhancing compounds (OECs) that promote endosomal leakage was explored. This strategy significantly improved the intracellular delivery of PMOs, confirming that endosomal entrapment is a major bottleneck within the whole delivery process.[23,31,32] Nevertheless, the clinical development of such combinations can be challenging due to differences in biodistribution and toxicity profiles of PPMOs and OECs.[31–34] As an alternative, we hypothesized that conjugation of a PMO to the amphiphilic S10 peptide, rationally designed to combine an endosomal leakage domain (ELD) and a CPP, could promote endosomal escape and improve intracellular delivery without the need for OECs.

In previous studies, we have demonstrated that S10 successfully enabled the delivery of proteins and peptides into lung cells after intranasal or intratracheal administrations to mice, ferrets, and rhesus monkeys.[35–37] Although co-administration of S10 with a biomolecule to airways is a straightforward approach, chemically conjugating S10 with its cargo could further improve delivery efficiency and biodistribution throughout the respiratory system. In the present work, we investigated conjugation strategies between S10 and biomolecules that involve permanent thiol-maleimide (SMal) and reducible disulfide (SS) bonds either directly or through a PEG linker. As a first step, S10 was conjugated to a previously described fluorescently labeled nuclear localization signal derivative (nls*) peptide,[36,37] which can be imported to the nucleus as a confirmation of a successful cytoplasmic delivery.[38] To demonstrate the therapeutic potential of S10 conjugates, we selected a PMO that functions as a splice switching-oligonucleotide (SSO), which restores the EGFP fluorescence from an EGFP RNA containing a beta-globin intron with an aberrant 654 splicing mutation.[23] A human cell line and transgenic mice expressing this EGFP-654 transcript were used to visualize and quantify the successful delivery of this PMO, named PMO(EGFP). With both biomolecules (nls* and PMO), we established that their conjugation to S10 leads to a significantly higher delivery percentage than the unconjugated mixture (S10 + nls*/PMO). Results also show that conjugation via the reducible SS bond through a PEG linker is the most advantageous conjugation strategy. Glutathione (GSH)-mediated reduction studies suggested that such conjugate behaves as a smart delivery molecule in which, the release of the biomolecule is triggered by the reducing agents present in cells.[39–41] Overall, we believe that our conjugation approach provides a great opportunity to push forward the clinical development of PMO-based therapies for lung diseases.

RESULTS

S10 efficiently enables the intracellular delivery of the sulfo-Cy5-labeled D-retro-inverso NLS (nls*) peptide *in vitro*

S10, composed of an ELD- and a CPP-derived domain (Figure 1A, left), has been shown to enable the intracellular delivery of biomolecules such as GFP, CRISPR-associated nuclease ribonucleoprotein (RNP), base editor RNP, and a fluorescent peptide into lung cells after intranasal or intratracheal administrations to different animal models.[35–37] Before investigating the conjugation reactions, we established the delivery conditions using previously described methods in which S10 was mixed with a D-retro-inverso NLS peptide (nls) fluorescently labeled via a SMal click reaction.[36,37] Briefly, an nls peptide, bearing a cysteine at the C-terminus side (nls-Cys), was reacted with a sulfo-Cy5-Mal (sCy5-Mal) fluorescent dye via a SMal click reaction to generate the fluorescently labeled nls-SMal-sCy5 (**nls***) as depicted in Figure 1A (right). Composed of D-amino acids,[42] this **nls*** is protease resistant and is actively transported to the nucleus once delivered to the cytoplasm.[38,43] In addition to these properties, this **nls*** has a

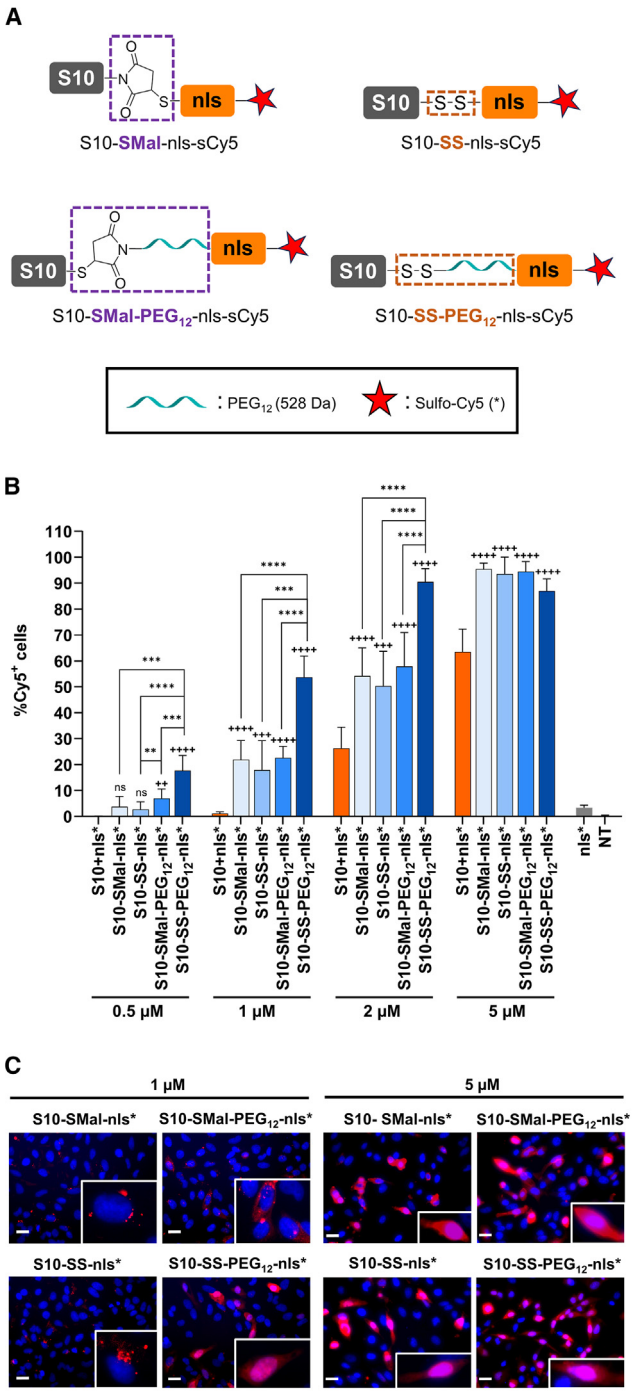

Figure 2. *In vitro* cellular uptake of conjugates in HeLa cells

(A) Structure of conjugates **S10-SMal-nls***, **S10-SMal-PEG-nls***, **S10-SS-nls***, and **S10-SS-PEG$_{12}$-nls***. (B) Dose-response of conjugates and cellular uptake measured by flow cytometry. Statistical significance was evaluated using a two-way ANOVA with Tukey's *post hoc* test. * and $^{+}$ $p < 0.05$, ** and $^{++}$ $p < 0.01$, *** and $^{+++}$ $p < 0.001$, **** and $^{++++}$ $p < 0.0001$ with * representing the comparison within conjugates and + (on top of the bars) representing the comparison between the conjugates and the corresponding control mixture (**S10+nls***). (C) Fluorescence live imaging of conjugates showing the internalized **nls*** at 20× magnification (scale bars, 30 µm) with Hoechst 33342 stained cell nuclei (blue) and **nls*** (red) using a Revolve R4 hybrid inverted fluorescence microscope. Results are expressed as means from replicates ± SD with $n = 3$.

molecular weight close to PMOs, which makes this peptide a suitable cargo model for our study. Cellular delivery of **nls*** at 7.5 µM was evaluated *in vitro*, either alone or mixed with S10 at 7.5 µM. Briefly, **nls*** was incubated with HeLa cells for 24 h (Figures 1B and S21–S23), whereas the **S10+nls*** mixture was incubated with cells only for 5 min before being washed and incubated for 24 h (Figure 1C). Microscopy images, taken at the beginning (0 h) and after 24 h of incubation, indicated that **nls*** did not penetrate cells after short exposure. However, a perinuclear sCy5^{+} signal was observed after 24 h of incubation (Figure 1B). In contrast, live imaging of cells incubated with the mixture containing S10 and **nls*** (**S10+nls***) shows sCy5^{+} cells after a 5-min incubation (0 h). Within this condition, fluorescence was mainly detected in the nucleus, indicating that S10 promoted the cytoplasmic delivery of **nls***, which was then efficiently imported to the nucleus (Figure 1C). As expected for a stable D-retro-inverso peptide, nuclear fluorescence did not decrease even after 24 h of incubation (Figures 1C and S22).[36,37] With such results, **nls*** represents a powerful tool to evaluate intracellular delivery over time and a suitable cargo model for the study of biomolecules with similar molecular weights, such as PMOs.

Conjugating S10 to nls* via a cleavable SS bond and a PEG$_{12}$ linker is highly efficient for the intracellular delivery of nls* *in vitro*

The delivery of **nls*** as a biomolecule in HeLa cells was successful when co-incubated with S10, as expected. Even though this strategy is very efficient, the biodistribution and fate of both compounds as separate molecules can differ, especially *in vivo*, where the mixture could be diluted in biological fluids. Hence, we hypothesized that covalently attaching S10 to a biomolecule should maintain the proximity of both entities at the cell surface and further improve delivery in a challenging environment like lung airways. Biomolecules, including PMOs, can be covalently attached to CPPs by direct conjugation or through short linkers (indirect conjugation).[26–29] To the best of our knowledge, there are no studies comparing direct and indirect conjugation of CPPs with biomolecules such as NLS peptides or PMOs. Thus, we investigated the conjugation of S10 to **nls*** via both conjugation strategies. Four S10-nls* conjugates were designed in this study. The first two conjugates consisted of directly linking S10 to **nls*** via a SMal permanent bond, or an SS bond, leading to S10-SMal-nls* (**S10-SMal-nls***) and S10-SS-nls* (**S10-SS-nls***), respectively, as shown in Figure 2A (top). The reducible SS bond aimed to investigate the release of the cargo via the oxidation and reduction system within the cellular environment.[41,44] The other two conjugates, S10-SMal-PEG$_{12}$-nls* (**S10-SMal-PEG$_{12}$-nls***) and S10-SS-PEG$_{12}$-nls* (**S10-SS-$_{PEG12}$-nls***), were prepared using the same chemical bonds (SMal and SS) but with a monodisperse polyethylene glycol (PEG$_{12}$; molecular weight = 528 Da) inserted as a linker between S10 and

nls* (Figure 2A, bottom), representing the indirect conjugation strategy. These last conjugates assessed the impact of extending the distance between both entities to potentially decrease the steric hindrance between S10 and the biomolecule. Conjugation reactions are described in the supplemental information (Section 1B). All conjugates were successfully obtained and were soluble in aqueous media, which made them suitable for *in vitro* studies.

To determine the best conjugation strategy, all conjugates were applied at different concentrations on HeLa cells for 5 min, after which cells were washed for further analyses. As a quantitative measurement of $sCy5^+$ cells, flow cytometry was performed 1 h after the 5-min incubation with cells (Figures 2B and S24). Each conjugate concentration was compared with the equivalent control mixture (**S10+nls***) at the same concentration with a 1:1 ratio to keep the same molarity as the conjugates. Results showed that all conjugates, at concentrations ranging from 0.5 to 5 μM, have higher delivery efficiency than their corresponding control mixtures (**S10+nls***), as shown in Figure 2B. It should be noted that below 0.5 μM of conjugates, fluorescence was under the detection limit, and above 5 μM, the maximum percentage of $sCy5^+$ cells was reached. Strikingly, data highlighted that conjugate **S10-SS-PEG$_{12}$-nls*** significantly outperformed the other conjugates at low concentrations (0.5–2 μM). This last conjugate achieved approximately 50% of cell fluorescence at 1 μM and reached a plateau corresponding with the maximum fluorescence (approximately 90%) at 2 μM, while the other conjugates could only achieve approximately 50% of cell fluorescence at 2 μM, even with **S10-SS-nls*** obtained through a similar reducible SS bond, underlining the benefit of the PEG_{12} linker (Figure 2B). At 5 μM, flow cytometry data indicated that all conjugates had reached the maximum fluorescence signal (Figure 2B). To investigate the cellular localization of the sCy5 signal, live microscopy was conducted. Cells treated with 1 μM of **S10-SS-PEG$_{12}$-nls*** displayed a strong nuclear fluorescence signal, an indication of successful delivery of the **nls*** (Figures 2C, left, and S25). Regarding the other conjugates at this concentration, cell fluorescence in the nucleus was hardly detected after delivery, as demonstrated by the absence of colocalization of the sCy5 signal with the Hoechst-stained nucleus, suggesting unsuccessful or inefficient cytoplasmic delivery. However, at 5 μM, live imaging showed nuclear fluorescence for all conjugates, indicating the successful intracellular delivery of the **nls*** at this concentration (Figures 2C, right, and S25). Nevertheless, with **S10-SS-PEG$_{12}$-nls*** enabling the delivery of **nls*** at lower concentrations, this conjugate remains the best candidate for further evaluation *in vivo*.

Assessment of the disulfide bond cleavage within S10-SS-nls* and S10-SS-PEG$_{12}$-nls*

S10-SS-nls* and **SS-PEG$_{12}$-nls*** conjugates contain the releasable SS bond that could potentially be cleaved by the reducing agents within cells. Yet, **S10-SS-PEG$_{12}$-nls*** outperformed **S10-SS-nls*** regarding delivery efficiency at low concentrations. Several studies investigating redox-responsive disulfide bonds have proved that direct conjugation of two active compounds often suffers from steric hindrance.[45] We believe that the PEG_{12} linker within **S10-SS-PEG$_{12}$-nls*** might have an impact on the SS bond cleavage in cells, which could also explain the *in vitro* results. To investigate this aspect, we evaluated SS bond reduction within both conjugates in the presence of GSH. GSH is one of the most abundant reducing agents in cells. The normal intracellular concentration of GSH ranges between 2 and 10 mM, whereas the extracellular concentration of GSH is only approximately 2–20 μM.[39,40] Thus, **S10-SS-nls*** and **S10-SS-PEG$_{12}$-nls*** were incubated with 20, 200, and 1000 μM of GSH, and ultra performance liquid chromatography (UPLC)/UV-mass spectrometry (MS) was carried out to monitor the SS bond cleavage from the conjugates over time. With both conjugates, even though complete SS bond cleavage could not be visualized due to overlapping UV signals, the rate of cleavage increased with increasing concentrations of GSH, leading to a decrease in the UV signal of the conjugates (Figures 3A–3C, S26A–S26C, and S26E–S26G). Note that no signal decrease was observed when conjugates with the SMal bond were incubated with GSH (Figures 3D, S26D, and S26H). Strikingly, incubation of **S10-SS-nls*** with 20 μM of GSH led to SS bond cleavage up to approximately 40% after 24 h, whereas the same incubation conditions with **S10-SS-PEG$_{12}$-nls*** led to SS bond cleavage of less than approximately 10% after 24 h (Figure 3A). A similar trend was observed at 200 and 1,000 μM of GSH, indicating that **S10-SS-PEG$_{12}$-nls*** is less sensitive to GSH-mediated reduction than **S10-SS-nls***.

Conjugate S10-SS-PEG$_{12}$-nls* efficiently delivers nls* to airway epithelial cells *in vivo* following intranasal instillation

Since S10 enabled the delivery of peptides and proteins into the airways of mice and ferrets after intranasal instillations,[35–37] we assumed that our conjugates could be administered via the same route and reach the airways. Given the *in vitro* performance of the conjugates compared with their control **S10+nls*** mixtures, we hypothesized that their intranasal instillation could improve the delivery efficiency and biodistribution throughout the airway by maintaining the proximity of S10 to the **nls***. With their sensitivity against cellular reducing agents, conjugates with an SS bond are preferable since the released biomolecule would have more freedom to exhibit its activity. **S10-SS-PEG$_{12}$-nls*** was identified as our best conjugate according to the *in vitro* data, However, in the context of lung delivery, the impact of the PEG linker within this conjugate in terms of SS bond cleavage kinetic and biomolecule delivery could not be predicted and needed to be investigated. Therefore, conjugates **S10-SS-nls*** and **S10-SS-PEG$_{12}$-nls*** were both evaluated in mouse lungs after a single intranasal instillation. The **nls***, as well as the **S10+nls*** mixture, were used as controls to respectively eliminate non-specific cell uptake and to assess the advantage of conjugation. Thus, single doses of **S10-SS-nls***, **S10-SS-PEG$_{12}$-nls***, and the control **S10+nls*** were intranasally instilled at 20 and 40 μM, as reported previously,[35] while **nls*** was administered only at 40 μM. Mouse lungs were harvested 24 h after delivery to limit the fluorescence background due to undelivered material (Figures S27A–S27C and S27F). The total fluorescence of the whole lung was first evaluated by *ex vivo* fluorescence imaging using an *in vivo* imaging system (IVIS). At 24 h after instillation, sCy5 fluorescence signal was observed throughout the respiratory tree ranging from the trachea to the whole lung (Figure 4A and S28).

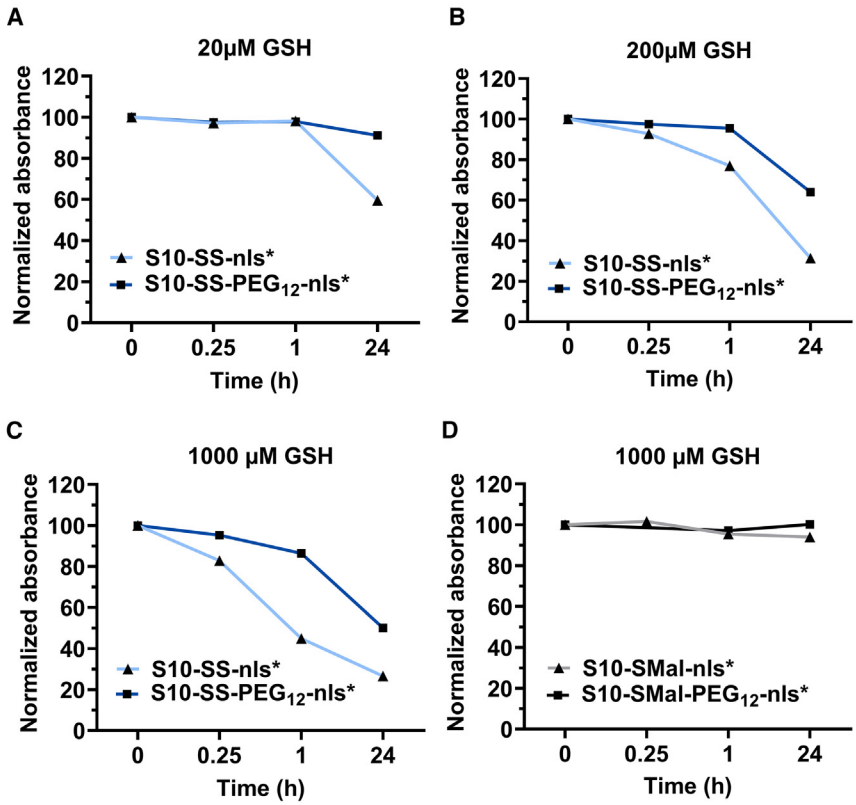

Figure 3. Release kinetics of disulfide bonds in conjugates S10-SS-nls*and S10-SS-PEG$_{12}$-nls* and maleimide bonds in conjugates S10-SMal-nls* and S10-SMal-PEG$_{12}$-nls* at different GSH concentrations

Level of release of the disulfide bond in conjugates **S10-SS-nls***and **S10-SS-PEG$_{12}$-nls***at four different timepoints in the presence of (A) 20 μM, (B) 200 μM, and (C) 1,000 μM GSH. (D) Level of release of the maleimide bond in conjugates **S10-SMal-nls*** and **S10-SMal-PEG$_{12}$-nls*** at four different timepoints in presence of 1,000 μM GSH.

Quantification of *ex vivo* total lung tissue fluorescence showed that lungs from mice administered with **S10-SS-PEG$_{12}$-nls*** led to a higher sCy5 signal compared with **S10-SS-nls*** (with a significant difference at 40 μM) or the controls **S10+nls*** and **nls*** (Figure 4B). Although a fluorescence signal from the whole lung is not necessarily indicative of intracellular delivery of the **nls*** in airway cells, it foreshows the presence and retention of our compounds within the lung. Hence, lungs from the mice treated with the conjugates and controls were sectioned, and histological examination was performed to quantify the sCy5 fluorescent signal and visualize the peptide localization within the cells from the trachea and the proximal and distal airways. In agreement with *ex vivo* imaging, **S10-SS-PEG$_{12}$-nls*** was significantly the most efficient at delivering the fluorescent biomolecule to epithelial cells among all formulations, with a percentage of sCy5$^+$ epithelial cells reaching approximately 20%–40% at 20 μM and 40%–60% at 40 μM. In addition, the fluorescent signal in the trachea and the proximal and distal regions of the lung was relatively similar, indicating a homogeneous distribution (Figures 4C–4E). With **nls*** alone, fluorescence was mostly observed in isolated cells, while **S10+nls***, **S10-SS-nls***, and **S10-SS-PEG$_{12}$-nls*** enabled intracellular delivery of the labeled **nls*** into epithelial cells in the trachea and within the whole lung airways (Figure 4F). To further characterize the lung delivery profile, immunofluorescent staining was conducted. The sCy5$^+$ cells, observed with **S10-SS-PEG$_{12}$-nls***, for instance, in the epithelium, were identified mostly as club cells (uteroglobin$^+$) and ciliated cells (α-tubulin$^+$), since both types of cells were double positive for the cell-specific marker and the sCy5 signal (Figure 4G). Since goblet cells are rare in the conducting airways of mice in the absence of inflammation,[46,47] the delivery to goblet cells was not examined. Immunofluorescence results also showed that the sCy5$^+$ isolated cells were macrophages (F4/80$^+$ cells) that have likely taken up free extracellular **nls*** (Figure 4G). Using flow cytometry analysis on digested whole lungs, we were able to define the relative proportion of delivered cells per cell type (Figure S29). With 40 μM, **S10+nls*** and **S10-SS-nls*** reached approximately 4%–7% of epithelial cells, while **S10-SS-PEG$_{12}$-nls*** enabled delivery to approximately 18% of epithelial cells (CD45$^-$CD326$^+$CD31$^-$) (Figures S27D and S27E). These results agree with the data obtained from *in vivo* image analysis. As the use of a 528 Da PEG (PEG$_{12}$) in S10-SS-PEG$_{12}$-nls* slowed down the kinetics of the SS bond reduction and improved the *in vitro* and *in vivo* delivery of the nls*, we investigated the effect of using a larger 7,500 Da PEG (PEG$_{170}$). We observed that increasing the size of the PEG linker led to a conjugate (S10-SS-PEG$_{170}$-nls*) that enabled the intracellular delivery of **nls*** in HeLa cells (Figures S30A–S30D), but required higher concentrations to reach the level of fluorescence obtained with all conjugates. Despite this successful intracellular delivery *in vitro*, intranasal instillation of this larger conjugate at 40 μM led to a fluorescent signal mostly detected in macrophages (Figure S31), as confirmed by F4/80 staining.

Overall, this study shows that conjugating S10 to the enzymatically stable **nls*** is more efficient when performed (1) via the cleavable SS bond allowing both entities to be released and (2) through a PEG linker with a moderate size that reasonably separates both entities, as demonstrated by **S10-SS-PEG$_{12}$-nls***, which was the most efficient conjugate *in vitro* and *in vivo*.

S10-PMO(EGFP) conjugates promote splice switching in HeLa-EGFP-654 cells

PMOs are interesting therapeutic biomolecules due to their ability to function as SSOs. Their FDA approval for DMD proves that PMOs can be translated to clinics.[16,18,48] While the combination of

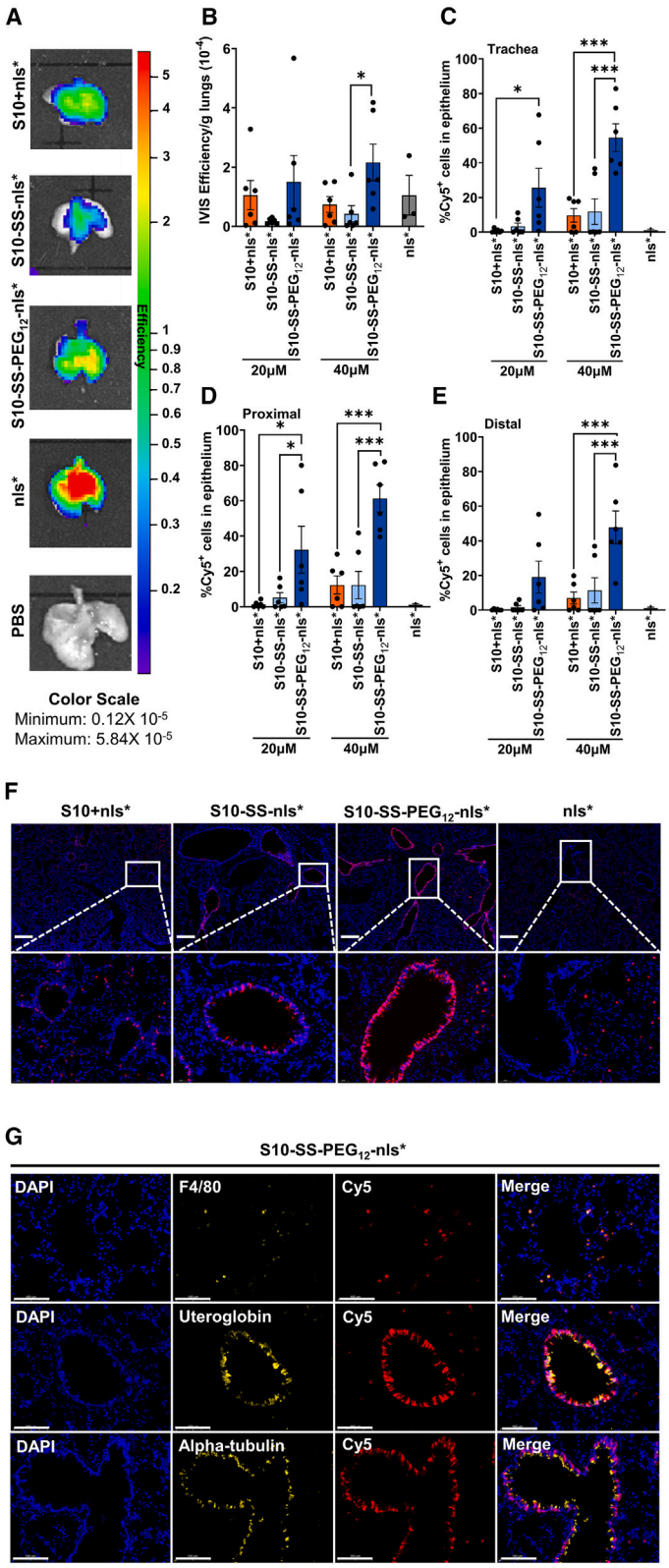

Figure 4. Quantification of cellular uptake in CD1 mice

A single dose of **nls***, **S10+nls***, **S10-SS-nls***, and **S10-SS-PEG$_{12}$-nls*** were administered to the mice by intranasal instillation. All mice were euthanized 24 h after instillation. (A) Representative images of *ex vivo* imaging of the whole lung using IVIS. (B) Quantification of total fluorescence efficiency. (C) Quantification of the percentage of sCy5^{+} cells in the epithelium of the trachea, (D) the proximal region of the lung, and (E) the distal region of the lung. (F) Representative slides of sCy5 delivery in the lung epithelium after administration of **nls***, **S10+nls***, **S10-SS-nls***, and **S10-SS-PEG$_{12}$-nls*** at 40 μM (scale bars, 300 μm). (G) Co-localization of sCy5 and F4/80 (macrophages), uteroglobin (club cells), and alpha-tubulin (ciliated cells) staining in mice treated with **S10-SS-PEG$_{12}$-nls*** at 40 μM (scale bars, 100 μm). Statistical significance was evaluated using a two-way ANOVA excluding the **nls*** alone with a Tukey's *post hoc* test. $^{*}p < 0.05$, $^{***}p < 0.001$. Results are expressed as means from replicates ±SEM with $n = 3$ (**nls***) and $n = 6$ (**S10+nls***, **S10-SS-nls***, and **S10-SS-PEG$_{12}$-nls***).

PPMOs and OECs is being explored, the clinical translation of such a two-compound formulation can be difficult due to their different fates *in vivo*.[31–34] Therefore, the development of effective PPMOs without OECs could be a major step toward the clinical translation of PMO-based lung therapies. With the delivery ability of S10, we hypothesized that S10-PMO(EGFP) conjugates could achieve such prowess. As a first step, we investigated the ability of S10 to deliver the PMO(EGFP) by mixing both entities as performed above for the labeled **nls***. For this purpose, intracellular delivery of the PMO(EGFP) was carried out in HeLa EGFP-654 cells, which stably express the EGFP reporter system. Following intracellular delivery, the PMO(EGFP) will reach and bind to the aberrant 654 splicing mutation within the EGFP RNA. This binding will lead to the translation of a functional mRNA leading to a fluorescent EGFP protein within 24 h,[49] as schematized in Figure 5A. Several studies suggest that PPMOs can be efficiently endocytosed but struggle to escape endosomal entrapment and eventually require high concentrations, potentially leading to toxicity.[50–53] Thus, to simultaneously monitor cellular uptake over time and EGFP fluorescence following splicing correction, the PMO(EGFP) was labeled with a fluorescent dye. Briefly, a PMO(EGFP) bearing a DBCO was designed and reacted to a sCy5-N_3 via strain-promoted alkyne-azide cycloadditions (SPAAC), resulting in the sCy5-labeled PMO (**PMO***), as depicted in Figure 5B. **PMO***, at 10 μM, was then incubated with HeLa EGFP-654 cells and monitored for 24 h. In parallel, the mixture **S10+PMO*** at 10 μM was incubated with the HeLa EGFP-654 cells for 5 min, after which, cells were washed and monitored for the following 24 h as described in the materials and methods section and in Figure 5C. Flow cytometry and live microscopy, monitoring sCy5 fluorescence, revealed that endocytosis of **PMO*** started 4 h after delivery and increased over time to reach approximately 98% of $sCy5^+$ cells after 24 h. However, the fluorescence was mostly perinuclear, and no nuclear fluorescence was observed (Figures 5D, S32, and S33). The absence of sCy5 fluorescence in the nucleus suggested that **PMO*** was endocytosed, but was mostly trapped in endosomes. When **PMO*** was mixed with S10, the resulting **S10+PMO*** mixture led to nuclear fluorescence (approximately 75% of sCy5-positive cells) immediately after the 5-min delivery (0 h). This nuclear sCy5 fluorescence persisted even after 24 h, indicating a successful intracellular delivery of **PMO***. In addition to sCy5 fluorescence monitoring, the functionality of the **PMO*** was evaluated by visualizing and quantifying the percentage of $EGFP^+$ cells (Figures 5E, S32, and S33). Results exposed the absence of $EGFP^+$ cells when incubated with **PMO*** alone, while the **S10+PMO*** mixture led to approximately 30% of $EGFP^+$ cells after 8 h. This percentage further increases to reach approximately 70% after 24 h. Overall, these results demonstrate that **PMO*** alone is efficiently internalized given the $sCy5^+$ cells after 24 h of incubation. Still, the absence of nuclear sCy5 fluorescence and EGFP expression confirms that, without S10, the PMO does not reach the pre-mRNA within the nucleus.

Next, S10 was attached to the **PMO** via SS bond either directly or through the PEG_{12} linker. Figure 6A displays the structures of S10-SS-PMO (**S10-SS-PMO**) and S10-SS-PEG_{12}-PMO (**S10-SS-PEG_{12}-PMO**), and details about the synthesis are described in the supplemental information. Briefly, **S10-SS-PMO** was obtained after reacting the thiol-activated S10 (S10-OPSS) to a PMO(EGFP) bearing a cysteine on its 3′ end. As for **S10-SS-PEG_{12}-PMO**, a bifunctional PEG_{12} bearing a DBCO and a thiol-activated OPSS (DBCO-PEG_{12}-OPSS) was reacted with a PMO bearing an azide on its 3′ end (PMO(EGFP)-N_3) via SPAAC. S10 was then linked on the other end of the bifunctional PEG_{12} via SS bond formation to yield conjugate **S10-SS-PEG_{12}-PMO**. Both conjugates were evaluated in HeLa EGFP-654 cells as described in the materials and methods section. Flow cytometry analyses and live imaging show that EGFP was efficiently expressed in delivered cells (Figures 6B, 6C, S34, and S35). The percentage of $EGFP^+$ cells obtained with both conjugates is significantly higher compared with the control mixture (**S10+PMO**) at lower concentrations. For instance, at 2 μM, both conjugates reached approximately 43% of $EGFP^+$ cells, while less than 1% was detected with the **S10+PMO** condition. As for the comparison between both conjugates, no significant difference was observed.

S10-PMO(EGFP) conjugates promote splice switching in lung cells of CAG-EGFP-654 mice after a single intranasal administration

The CAG-EGFP-654 mice are reporter mice used to track alternative splicing manipulation. Like the HeLa-EGFP-654 cells, these mice ubiquitously express an EGFP-654 system to report the PMO(EGFP) SSO activity. Building upon the *in vitro* results, we performed quantitative *in vivo* studies involving **S10-SS-PMO** and **S10-SS-PEG_{12}-PMO**. Following intranasal instillation of the PMO alone, there were very few cells expressing EGFP (Figure 7) as expected, due to its low cell permeability. At 40 μM, the percentage of cells expressing EGFP in the pulmonary epithelium increased substantially when **S10-SS-PMO** and **S10-SS-PEG_{12}-PMO** were administered, with levels reaching 3%–5% of total epithelial cells by flow cytometry and up to 45% of bronchial epithelial cells by immunofluorescence, as shown in Figures 7A–7D and S36. Consistent with the *in vitro* results, no difference in EGFP expression between both conjugates was observed, and fluorescence was relatively homogeneous in the proximal and the distal regions of the lungs. Like conjugates with the **nls***, the EGFP-expressing epithelial cells were identified as club cells (uteroglobin$^+$) and ciliated cells (α-tubulin$^+$), and the fluorescent isolated cells in the lung parenchyma were macrophages as characterized by immunofluorescence (Figure 7E).

To discriminate between the cells that received the PMO without EGFP expression and the cells expressing EGFP due to mediated splicing corrections, **S10-SS-PMO** was labeled with sCy5. To achieve such labeling, we designed a new bifunctional PMO(EGFP) bearing a thiol on its 3′ end and a DBCO on its 5′ end. Conjugation via SS bond to S10 was performed on the 3′ end, while labeling of the PMO(EGFP) was carried out on the 5′ end by SPAAC with a sCy5-N_3, resulting in **S10-SS-PMO*** (Figure 8A, details in supplemental information Section 1Bs and 1Bt). **S10-SS-PMO***, at 1 and 2 μM, was first evaluated *in vitro* in HeLa EGFP-654 cells. Results show that EGFP and sCy5 fluorescence are colocalized in most cells, with an intensity that is

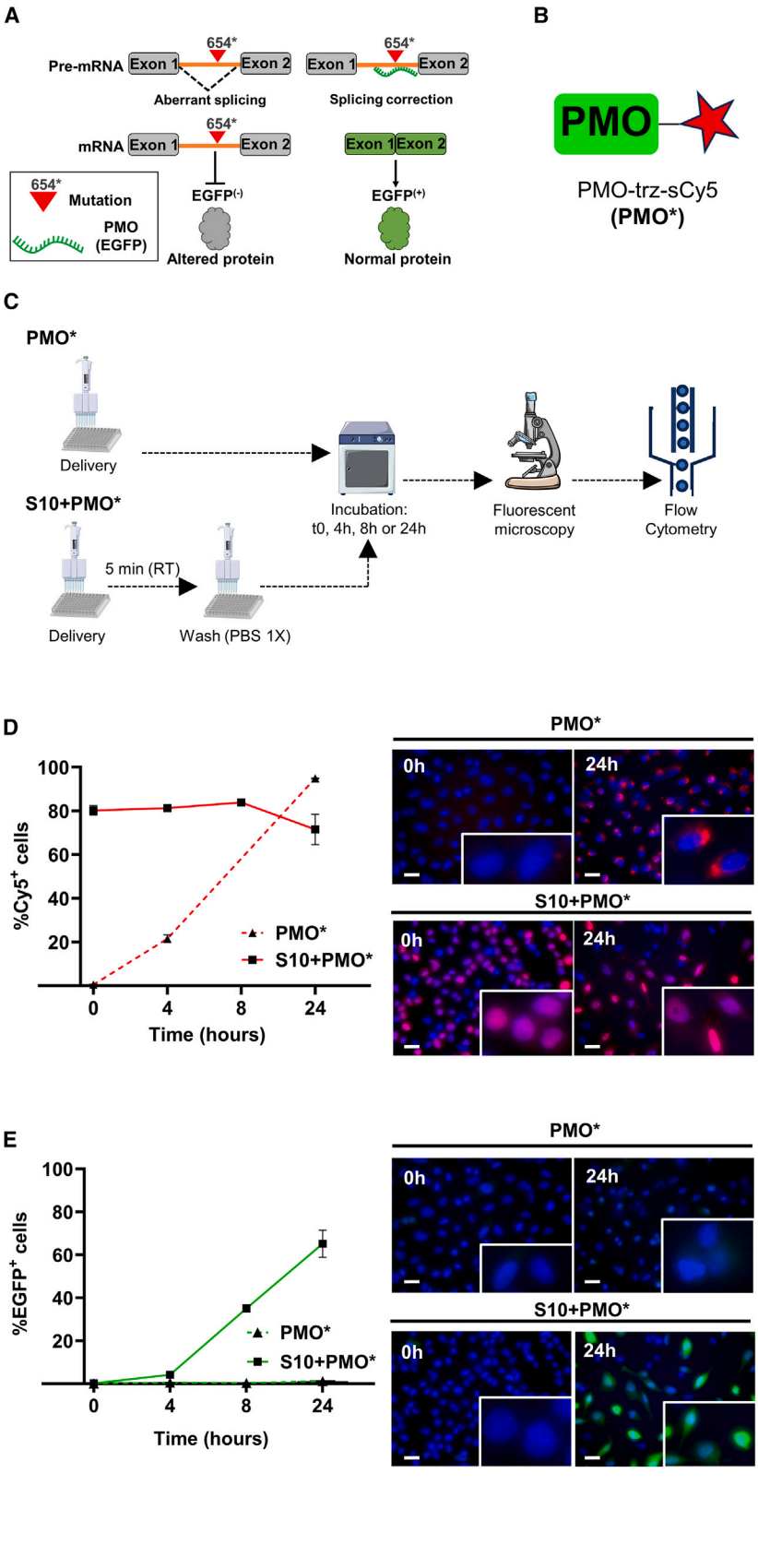

Figure 5. Splicing correction and restoration of EGFP expression in HeLa EGFP-654 using S10 delivery agent and PMO*

(A) Scheme of the EGFP-654 assay showing, on the left, the EGFP construct with the 654-mutation introduced in the intronic region of the EGFP gene which leads to intron retention and aberrant splicing (dashed lines). On the right, the PMO(EGFP) mediated splice-switching and reestablishment of an intact EGFP mRNA and translation of a functional protein expression. (B) Chemical structure of **PMO***. (C) Schematic of the delivery experiments for **PMO*** and **S10+PMO*** mixture and its incubation period before live imaging microscopy and flow cytometry. (D) Time course of cellular uptake and localization of **PMO*** with and without S10 analyzed by flow cytometry and live microscopy. Hoechst 33342-stained nuclei are in blue and **PMO*** in red. (E) Functional evaluation of free cellular uptake and S10 delivered **PMO*** in HeLa EGFP-654 cells analyzed at different time points by flow cytometry quantification of $EGFP^+$ expressing cells and live microscopy (Hoechst 33342 nuclei in blue, EGFP in green) using a Revolve R4 hybrid inverted fluorescence microscope (scale bars, 30 μM). Results are expressed as means from replicates ± SD with $n = 3$.

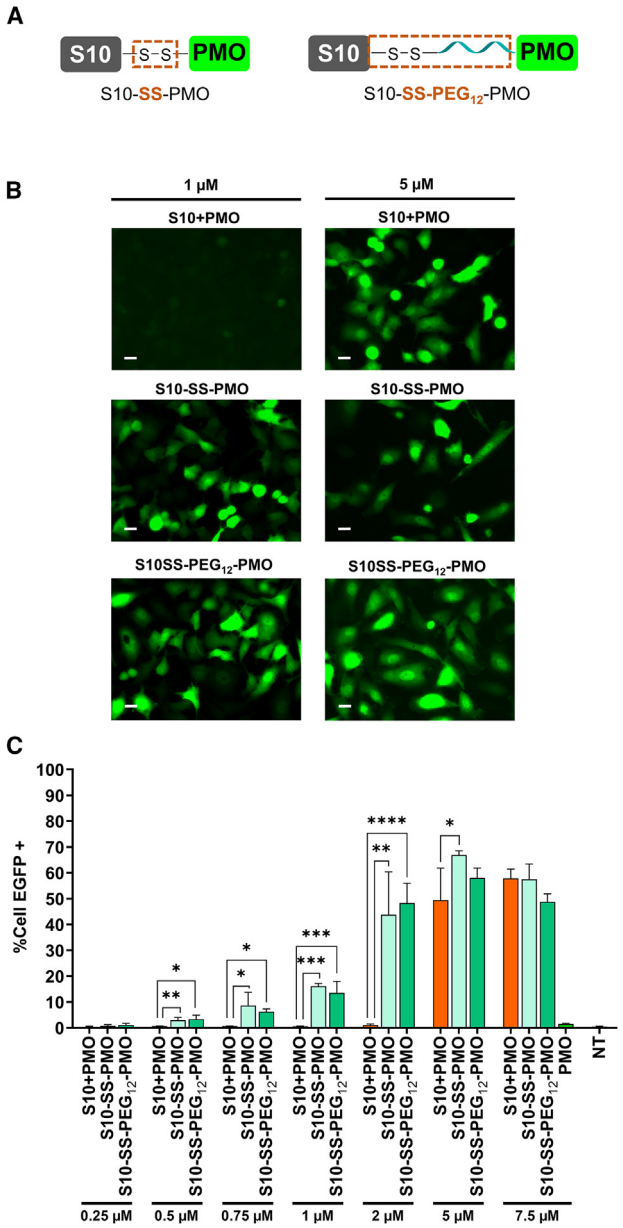

Figure 6. Evaluation of the splice-switching mechanism and EGFP fluorescence in HeLa-EGFP-654 cells induced by the PMO-related formulations

(A) Structure of conjugates **S10-S10-SS-PMO** and **S10-SS-PEG$_{12}$-PMO**. (B) Fluorescence live imaging of conjugates and the mixture **S10+PMO** showing the EGFP fluorescence at 20× magnification using a Revolve R4 hybrid inverted fluorescence microscope (scale bars, 30 μM). (C) Dose-response of conjugates measured by flow cytometry. Statistical significance was evaluated using a two-way ANOVA with Tukey's *post hoc* test. *$p < 0.05$, **$p < 0.01$, ***$p < 0.001$, ****$p < 0.0001$. Results are expressed as means from replicates ± SD with $n = 3$.

significantly higher than the control PMO* (Figures 8B, S37, and S38). Intranasal administration of **SS-PMO*** demonstrated that cells receiving the PMO mainly express EGFP, suggesting an efficient cytosolic delivery of the conjugate (Figure 8C). We also observed a few cells that are EGFP$^+$ but sCy5$^-$ (Figure 8B, zoomed-in regions), suggesting that splice switching and EGFP expression are more sensitive than sCy5 fluorescence measurement.

DISCUSSION

S10 is an amphiphilic peptide that rapidly and efficiently enables the intracellular delivery of various biomolecules, both *in vitro* and *in vivo*. The delivery process consists of mixing S10 with the biomolecule, which after *in vivo* administration, leads to a successful delivery to the targeted cells, tissues, or organs. In agreement with these data, **nls*** internalization mostly led to a perinuclear signal after 24 h incubation (Figure 1B), likely due to endosomal entrapment, whereas the **S10+nls*** mixture led to nuclear fluorescence within a 5-min incubation (Figure 1C), indicating successful intracellular delivery. While this strategy is efficient and straightforward, we demonstrated that covalently attaching S10 to **nls*** resulted in conjugates (Figure 2A) that led to a higher percentage of sCy5$^+$ cells compared with the **S10+nls*** mixture (Figure 2B). Among the conjugates, **S10-SS-PEG$_{12}$-nls*** emerged as the most efficient, outperforming the other conjugates at concentrations ranging from 0.5 to 2 μM. Strikingly, live imaging showed that, at 1 μM, **S10-SS-PEG$_{12}$-nls*** was the only conjugate that led to nuclear fluorescence after delivery, whereas a perinuclear fluorescent signal was mostly observed with the other conjugates (Figure 2C). Due to its amphiphilic nature, S10 is prone to interact with cell membranes. Thus, **S10-SMal-nls*** and **S10-SMal-PEG$_{12}$-nls***, obtained via permanent conjugation, could remain trapped in lipid bilayer components (cell membrane or endosomes) along with S10 at these concentrations, preventing the **nls*** from reaching the nucleus. In this context, conjugation via a disulfide bond seems crucial for the conjugate-mediated intracellular delivery of the **nls***, at least at 1 μM. Yet, in comparison with **S10-SS-PEG$_{12}$-nls***, **S10-SS-nls*** mainly resulted in a low perinuclear sCy5$^+$ signal, highlighting the impact of the PEG$_{12}$ linker. To further investigate this aspect, we conducted SS bond cleavage within the conjugates. GSH-mediated cleavage studies demonstrated that **S10-SS-PEG$_{12}$-nls*** was more resistant to SS bond reduction than **S10-SS-nls*** (Figure 3). Considering that the concentration of GSH in the cellular environment is approximately 1,000 times higher in the intracellular space, we think that SS bond reduction within **S10-SS-PEG$_{12}$-nls*** efficiently occurs once the internalization process is initiated. In contrast, with **S10-SS-nls***, the reduction could begin in the vicinity of the cell membrane in the extracellular environment. Hence, **S10-SS-nls*** would partially behave as the mixture **S10+nls***, which was more efficient at higher concentrations (5 μM). In contrast, **S10-SS-PEG$_{12}$-nls*** could function as a smart delivery conjugate, releasing the **nls*** only at high intracellular concentrations of a reducing agent, such as GSH. As for the nuclear fluorescence observed with **S10-SMal-nls*** and **S10-SMal-PEG$_{12}$-nls*** at 5 μM, we believe these conjugates simultaneously function as both a delivery agent and a cargo that can be delivered to the cytoplasm. With such a high concentration of conjugates, cell membranes could become saturated, allowing the remaining free conjugates within the cellular environment to reach the cytoplasm as cargos without being trapped in the lipidic

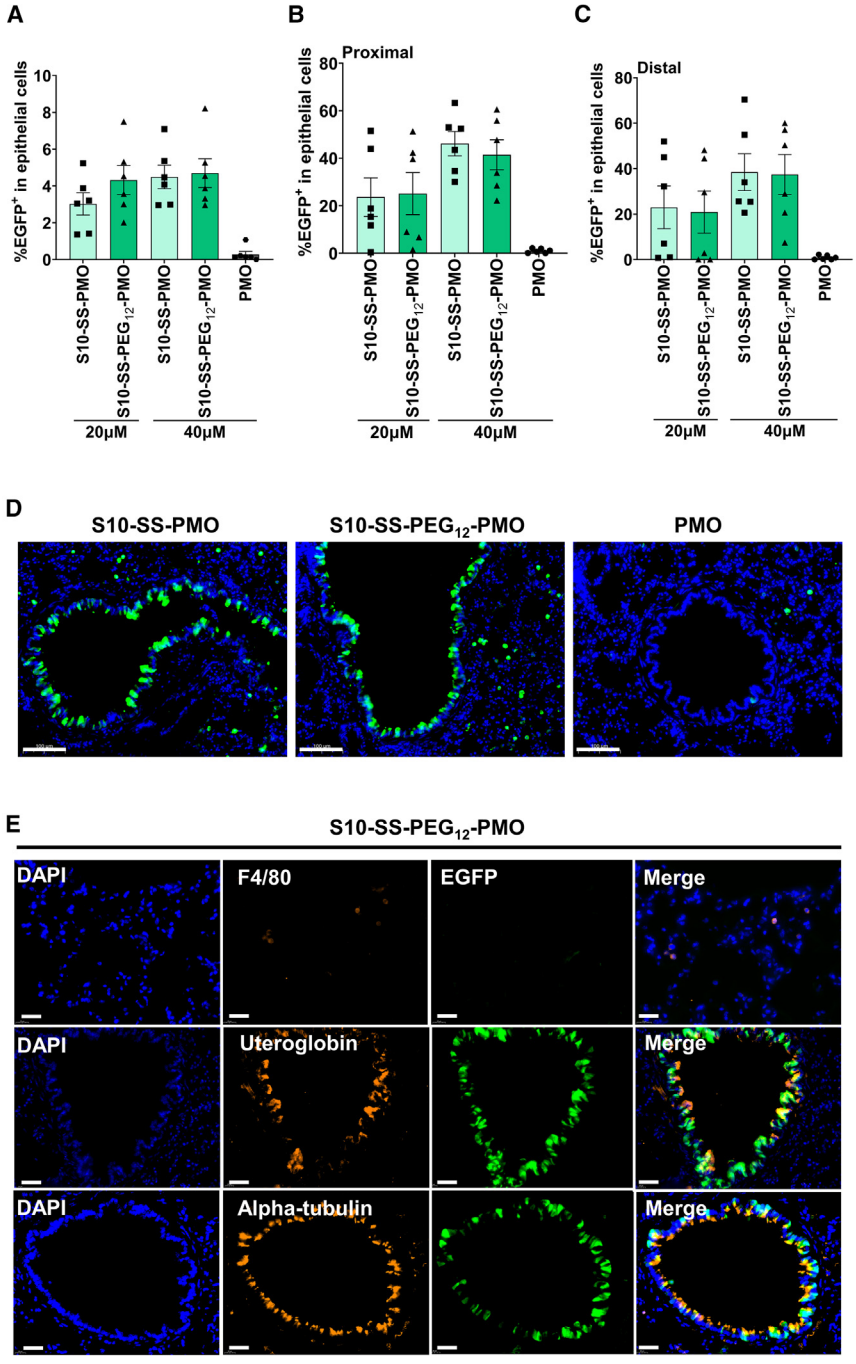

Figure 7. Quantification of cellular uptake of PMO(EGFP) and S10-PMO(EGFP) conjugates in CAG-EGFP-654 mice

The PMO(EGFP) alone, **S10-SS-PMO**, and **S10-SS-PEG$_{12}$-PMO** were administered by intranasal instillation. The mice were euthanized 72 h after administration. (A) The percentage of EGFP$^+$ epithelial cells in the whole lung measured by flow cytometry. (B) The percentage of EGFP$^+$ cells in the epithelium of the proximal region and (C) the distal region of the lung were quantified by EGFP immunofluorescence. (D) Representative slides of the PMO delivery in the epithelium following administration of S10-PMO(EGFP) conjugates and the PMO alone at 40μM (scale bars, 100 μm). (E) The co-localization of the EGFP and F4/80 (macrophages), uteroglobin (club cells), and alpha-tubulin (ciliated cells) staining in the mice treated with conjugate **S10-SS-PEG$_{12}$-PMO** at 40 μM (scale bars, 30 μm). Results are presented using means ± SEM. Statistical significance was evaluated using one-way ANOVA with Tukey's *post hoc* test. $^*p < 0.05$, $^{**}p < 0.01$, $^{***}p < 0.001$, $^{****}p < 0.0001$. Results are expressed as means from replicates ±SEM with $n = 6$.

membrane. We think that such a phenomenon could occur with all conjugates at high concentrations which can bias the comparative study. Hence, conjugate efficiency should be evaluated at low concentrations which outlined the potency of **S10-SS-PEG$_{12}$-nls***. Thus, *in vivo* studies were only carried out with **S10-SS-nls*** and **S10-SS-PEG$_{12}$-nls***, which assessed the impact of the PEG linker. Compared with **nls***, **S10+nls***, and **S10-SS-nls***, the **S10-SS-PEG$_{12}$-nls*** conjugate was significantly the most efficient at delivering the **nls*** to epithelial cells such as club and ciliated cells, highlighting the benefit of the conjugation via an SS bond through a PEG linker. We believe our conjugation strategy is well tailored for the S10 peptide given its strong hydrophobic interactions with membrane lipids and the need to release the cargo from these interactions to freely travel within the cell and perform its biological function. Applying the same conjugation strategy with other peptide-based delivery agents could be less efficient. For instance, the well-known TAT and (RXR)$_4$XB (with X = 6-aminohexanoic acid or Ahx, and B = beta-alanine or β-Ala) CPPs,[23,54–59] were conjugated to the nls* via an SS bond through a PEG$_{12}$ linker to give respectively TAT-SS-PEG$_{12}$-nls* and (RXR)$_4$XB-SS-PEG$_{12}$-nls* (Figures S39–S42) as performed for the synthesis of S10-SS-PEG$_{12}$-nls*. *In vitro* evaluation of the conjugates at 2.5, 5, and 7.5 μM for the delivery of nls* was performed using the 5-min delivery protocol. Results showed a strong nuclear fluorescence with S10-SS-PEG$_{12}$-nls* whereas no/low fluorescence was detected with the CPP-based conjugates after the 5-min delivery (Figure S43). Comparable results were obtained when comparing the non-conjugated delivery peptides (S10 vs. CPPs) (Figure S44), demonstrating the delivery efficiency of S10 over the two other CPPs in our delivery conditions. As supported by other studies, longer incubation times (1–4 h) are required for these CPPs to efficiently promote cargo delivery in cells (Figures S45 and S46). The presence of an ELD domain in S10 provides an alternative delivery

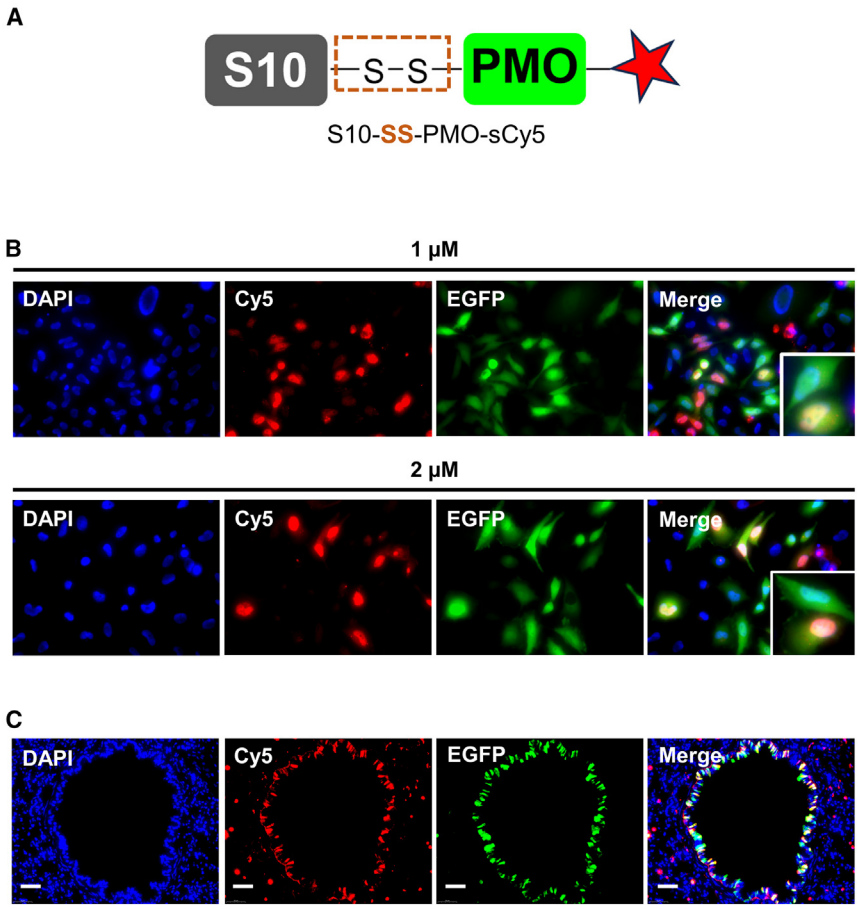

Figure 8. Colocalization of EGFP and sCy5 fluorescence in HeLa-EGFP-654 cells and in CAG-EGFP-654 mice after delivery of S10-SS-PMO*

(A) Structure of **S10-SS-PMO***. (B) Fluorescence live imaging of **S10-SS-PMO*** at 1 µM and 2 µM in HeLa-EGFP-654 cells. (Hoechst 33342-stained nuclei in blue, **S10-SS-PMO*** in red and EGFP in green) at 20× magnification using a Revolve R4 hybrid inverted fluorescence microscope (scale bars, 30 µM). (C) Representative slides of EGFP delivery in the epithelium of CAG-EGFP-654 mice following administration of **S10-SS-PMO*** at 40 µM (scale bars, 100 µM).

mechanism compared with CPPs, which could explain such results. Therefore, attaching a peptide-based delivery agent to a cargo needs a careful understanding of its delivery mechanism to design the best conjugation strategy. In our case, conjugation via an SS bond through a PEG_{12} linker was beneficial. Notably, the size of the PEG linker within the conjugate seems crucial since an increase in PEG size from PEG_{12} (528 Da) to PEG_{170} [7,500 Da] was detrimental *in vivo*, despite the moderate efficiency of this larger conjugate observed *in vitro*. Instead, fluorescence was predominantly detected in isolated cells, which were identified as macrophages (Figure S31). There is an increasing concern about PEG molecules regarding their safety, but this depends on several parameters, including their size. PEGs of moderate size (3,000–20,000 Da) could trigger an allergic or an immune response, whereas smaller PEGs exhibit a lower immune response.[60–63] Although immunogenicity was not fully investigated in the present work, F4/80 staining revealed a number of macrophages that were visually higher with this larger conjugate compared with conjugates with a smaller PEG, which agrees with previous studies. We believe that the absence of delivery to the airway epithelium is due to the larger size of the cargo moiety within the conjugate containing the PEG_{170}. While S10 can deliver substantially larger cargo than itself using a co-incubation protocol,[35–37] the direct conjugation of this PEG_{170}-nls* cargo (3 times larger than S10) might physically interfere with the cell binding and/or internalization process mediated by S10.[64] Consequently, administration of this large conjugate resulted in the accumulation of undelivered material in the airways which led to macrophage absorption, but further investigation is needed to support this hypothesis.

Switching the biomolecule from the **nls*** to the PMO(EGFP) further highlighted the potential of our S10-based conjugation strategy. *In vitro* experiments revealed that the **PMO** alone was non-functional in HeLa-EGFP-654 cells, whereas the conjugates **S10-SS-PMO** and **S10-SS-PEG_{12}-PMO** led to EGFP expression that significantly surpassed the results obtained with the **S10+PMO** mixture at low concentrations. Both PMO conjugates led to a similar EGFP expression, which was surprising given that conjugation through a PEG_{12} linker had outperformed the direct conjugation when using the **nls*** as a cargo. We believe that a low concentration of intracellular **PMO** is sufficient to mediate splicing correction, making discrimination between **S10-SS-PMO** and **S10-SS-PEG_{12}-PMO** undetectable by fluorescence-based assays. Intranasal instillation in CAG-EGFP-654 mice further confirmed the *in vitro* data with **S10-SS-PMO** and **S10-SS-PEG_{12}-PMO** delivering the cargo to approximately half of the bronchial epithelial cells. Regarding the biodistribution profile, cargo delivery from S10-SS-PMO and S10-SS-PEG_{12}-PMO was homogeneous throughout the lung, with EGFP-expressing epithelial cells predominantly being club cells and ciliated cells, similar to S10,[35,36] and conjugates S10-SS-nls* and S10-SS-PEG_{12}-nls*. Such data suggest that delivery using our conjugation strategy is independent of the biomolecule but is rather mediated by S10. Labeling the conjugate S10-SS-PMO with sCy5 (S10-SS-PMO*) further showed that most $sCy5^+$ cells also expressed EGFP both *in vitro* and *in vivo*, highlighting the efficiency of the conjugates. In terms of potential therapies, club cells, and ciliated cells are involved in pulmonary diseases such as CF and chronic obstructive pulmonary disease (COPD),[65–68] emphasizing the potential of our conjugation strategy to address such disorders. To the best of our knowledge, this is the first study showing that intranasal

administration of peptide PMOs is a suitable approach for the development of drugs against disorders that involve club and ciliated cells in the lungs. The most similar approach was performed by Dang and coworkers which demonstrated that a combination of a CPP-PMO(EGFP) and an OEC (UNC7938) could lead to mRNA splicing in mice lungs, but the formulation was administered intravenously. Although a direct comparison cannot be made due to the difference in the administration routes, we show that our approach requires less material (0.5–2 mg/kg vs. 12–15 mg/kg), avoids the use of OECs, and limits systemic exposure, making it potentially more convenient for the development of lung therapies.[35,36]

In conclusion, our approach showed that conjugating S10 to biomolecules such as peptides and PMOs via SS bond is a viable delivery method that bypasses endosomal entrapment, which is the main struggle in therapeutic ASO delivery. We further showed that inserting a PEG_{12} linker between S10 and the biomolecule can be beneficial. The size of the PEG linker seems to influence lung delivery efficiency. Studies investigating the impact of PEG linker size on cargo delivery *in vivo* could give insights into the mechanism behind this phenomenon while providing a more precise guideline for a versatile conjugation strategy between S10 and biomolecules of moderate sizes. In addition, delivery in club and ciliated cells shows the potential of such conjugates in biomolecule delivery to airway epithelia. Furthermore, *in vivo* delivery in these cells is interesting as they are involved in several pulmonary diseases, such as COPD, and CF, among others.[65–67,69–73] Thus, enabling the functional delivery of PMO to airway cells presents an attractive opportunity for the development of treatments for a wide range of pulmonary diseases. Considering that lung diseases rank among the top three leading causes of global mortality,[1,2,74,75] our approach provides a promising strategy to improve the cellular delivery of therapeutic biomolecules in lungs, which could potentially guide the development of ASO-based drugs against pulmonary diseases.

MATERIALS AND METHODS

Materials

Acetonitrile was purchased from Laboratoire Mat Inc. Formic acid and aldrithiol-2 (DPDS), Tris(2-carboxyethyl)phosphine hydrochloride (TCEP) were purchased from Millipore Sigma. GSH was purchased from BioShop. Monodisperse PEGs (SDPD-$dPEG_{12}$-NHS-ester, mal-$dPEG_{12}$-DBCO), and amine-DBCO were obtained from Quanta Biodesign. OPSS-PEG7.5kDa-SCM was purchased from Biopharma PEG. Sulfo-Cy5-Mal (sCy5-Mal), sulfo-Cy5-DBCO (sCy5-DBCO), and Sulfo-Cy5-azide (sCy5-N_3) were purchased from Lumiprobe. All peptides (, Cys-nls, nls-Cys, nls (Cys)-N_3, S10, and S10-Cys) were purchased from Expeptise. PMO, PMO-Cys, PMO-N_3, and HS-PMO-(DBCO) were obtained from Wuxi. Peptide and PMO sequences are listed in Table S1. DMEM, RPMI 1640 media, and fetal bovine serum (FBS) were obtained from Multicell. Penicillin (50 U/mL), streptomycin (50 μg/mL), L-glutamine (PSG, Fisher MT30009CI), Puromycin (500 ng/mL, InvivoGen), trypsin 0.05% (Corning Life Sciences), PBS 1× (homemade using standard protocol), Hoechst 33342 (Invitrogen, Thermo Fisher Scientific). HeLa (human cervical carcinoma cells) were purchased from the American Type Culture Collection (Ref. CCL-2).

Synthesis

Details about the synthesis and characterization of all compounds are described in the supplemental information and general methods are presented below.

General method A

Disulfide bond reduction (monomerization). All compounds bearing a cysteine were reduced with TCEP to break all remaining disulfide bonds and ensure their monomeric state before any further reaction. Reactions were monitored by UPLC, and final compounds were purified by preparative high-performance LC (HPLC) and characterized by LCMS.

General method B

Activation of thiol groups. Thiol activation was performed by reacting DPDS with free thiol groups. Reactions were monitored by UPLC, and final compounds were purified by preparative HPLC and characterized by LCMS.

General method C: Cargo labeling

For cargo labeling, SMal click and copper-free SPAAC reactions were performed. The reactions were monitored by UPLC. All compounds were purified by preparative HPLC and characterized by LCMS.

Synthesis of conjugates

S10 was conjugated to cargoes (nls and PMO) with and without a monodisperse PEG_{12} linker between both entities. For the direct conjugation (without the PEG_{12} linker), S10 was conjugated to the cargo via a SMal click reaction or a disulfide bond formation. In both cases, the reaction was monitored by UPLC, purified by HPLC, and characterized by LCMS. Regarding the conjugates with a PEG_{12} linker, S10 was first PEGylated using the bifunctional PEGs (OPSS-PEG_{12}-DBCO, and Mal-PEG_{12}-DBCO) via the same reactions. Both intermediates were then purified by preparative HPLC, characterized by LCMS, and further reacted with the cargos via SPAAC. Final products were purified by preparative HPLC or FPLC and characterized by LCMS.

GSH-mediated disulfide bond cleavage

Disulfide bond cleavage of conjugates **S10-SS-nls*** and **S10-SS-PEG_{12}-nls*** was evaluated using GSH as a reducing agent. Conjugates **S10-SMal-nls*** and **S10-SMal-PEG_{12}-nls*** with the SMal bonds were used as negative controls. Conjugates at 250 μM were solubilized in phosphate buffer (pH 7.4) and mixed in a solution of GSH at 40 μM, 400 μM, or 2 mM at a volume ratio of 1:1, giving mixtures containing 20 μM, 200 μM, or 1,000 μM of GSH and 125 μM of conjugates. At each time point, the cleavage of the disulfide bond within the conjugates was monitored by UPLC. Each chromatogram was normalized using the maximum absorbance of the conjugate. The decrease of the signal corresponding with the conjugates was integrated to quantify the percentage of disulfide bond cleavage over time (Figures 3 and S26).

Cell culture

HeLa cells were cultured in DMEM, supplemented with 10% FBS and 1% PSG (penicillin, streptavidin, and gentamicin), and were used to investigate the delivery of fluorescent cargos. To study the delivery of the functional PMO(EGFP), an SSO-inducible HeLa EGFP-654 cell line was generated by nucleofection (Lonza 4D Nucleofector) of an EGFP-654 expression cassette at the AAVS1 locus.[76] Briefly, wild-type HeLa cells were co-transfected via electroporation with a plasmid coding for a Cas9 and a guide RNA targeting the AAVS1 locus, along with a donor plasmid containing a puromycin-resistant gene, an EGFP-654 reporter cassette, and a homology arms to the AAVS1 locus sequence (OriGene Technologies, CAT#: GE100023 and customized GE100024). Cells were selected for puromycin resistance and single clones were isolated, validated, and used for *in vitro* functional delivery of PMO studies. To ensure the stability of the HeLa EGFP-654 cell line, cells were cultured in DMEM supplemented with 10% FBS, 1% PSG, and puromycin (500 ng/mL).

Cell delivery assay

One day before delivery, cells were seeded in a 96-well plate (20,000 cells/well) and allowed to attach for at least 16 h at 37°C in 5% CO_2 before testing. A nuclei stain was performed using 0.2 μg/mL of Hoechst 33342 per well. Cells, protected from light, were incubated for 30 min at room temperature, before delivery. Cells were then washed with sterile PBS 1× and incubated for 5 min at room temperature with the delivery mixtures (50 μL per well) S10 + cargo, S10-cargo conjugates, or cargo alone prepared in RPMI media at specific concentrations. Following the 5-min incubation, 100 μL of complete DMEM was added to each well to dilute and inactivate the shuttle's activity. Cells were finally washed with PBS 1× and incubated with a fresh complete DMEM and incubated for 1 h at 37°C in 5% CO_2 before flow cytometry and microscopy analyses.

Animals

Male CD1 mice (strain #022) were obtained at 6–7 weeks old from Charles River Laboratories. FVB CAG-EGFP*1Rkol/RjulJ (Strain #027617) were obtained from Jackson Laboratory and bred homozygously for the animal under experimental protocols. These mice express the EGFP protein coding sequence interrupted by the intron of human beta-globin encoding the 654-splicing mutation. The mutant EGFP RNA is expressed in all cell types, but is nonfunctional. Upon splicing correction with an ASO, functional EGFP is expressed.[23,76] Both male and female mice aged 6–8 weeks were used for the studies. This study was approved by the Cégep de Lévis Animal Care Committee (#003–21 and #008–21) and complied with CACC standards and regulations governing the use of animals for research. Five microns filtered, activated-charcoal treated, reverse-osmosis-treated tap water was provided to the animals. A standard certified commercial rodent diet (Envigo 2018) was also provided *ad libitum*, except during designated procedures requiring the handling of animals. For intranasal administration, mice were anesthetized by isoflurane inhalation (2.5%–4%) before instillation. Instillations were conducted with 50 μL of delivery mixtures per animal according to the respiratory rhythm. Treatment was administered dropwise while alternating nostrils between each drop. Mice were then turned on their back while slightly massaging their thorax for about 10 s before returning them to their housing. Animals were euthanized by cardiac puncture under isoflurane anesthesia 1, 24, or 72 h after instillation, respectively, for CD1 and CAG-EGFP-654 mice. After euthanasia, mice were tracheotomized and the lungs were washed with three times 1 mL PBS, with the last lavage being left in the lung for inflation. Two lobes from the right lung were collected, placed in a tube with 0.5 mL PBS, and stored on ice for flow cytometry analysis. The left lung and the trachea were collected and weighed for *ex vivo* imaging and microscopy.

Ex vivo imaging

The left lung and the trachea were transferred to a Petri dish and imaged using an *in vivo* imager (IVIS Lumina XR, PerkinElmer). The fluorescence level of the whole lung was determined using the Cy5 filter set (646/662 nm Ex/Em). The fluorescence level was measured using the total fluorescence efficiency and the result was normalized using the weight of the tissue.

Measurement of cargo uptake by flow cytometry

In vitro delivery efficiency analysis was performed 1 h post-delivery for all sCy5 fluorescent cargoes and 24 h after delivery for the EGFP expression in SSO-inducible HeLa EGFP-654 cells. For flow cytometry sample preparation, media was first removed from each well, and cells were washed with PBS 1×, then trypsinized for 10 min at 37°C in 5% CO_2 using 50 μL 0.05% trypsin per well to detach all cells. Cells were then resuspended in 100 μL of complete DMEM, to inactivate the trypsin. A total of 150 μL per cell suspension was transferred to a transparent U-bottom 96-well plate for flow cytometry analysis to determine the percentage of positive fluorescent cells and their emitted signal intensity (Cytoflex, Beckman Coulter). Briefly, the percentage of cells with a fluorescence signal greater than the maximum fluorescence of untreated cells was used to identify positive fluorescent cells and determine the delivery efficiency. Furthermore, the size and granularity measures of the cells from the cytometer allowed for the determination of cellular toxicity for all the cargoes (% cell viability by comparing the size and granularity (SSC) of each delivered cell condition to its untreated control). All *in vitro* viability measurements are provided in the supplemental information (Figures S23–S37).

For *in vivo* studies, the lungs were minced with surgical scissors and a 2× digestion mix composed of 0.2% collagenase type IV (Fisher Scientific, cat. num. NC9919937) and 0.04% DNase I (Sigma Aldrich, cat. num. DN25, 100 mg) was added to the lung. The tissues were digested for 1 h at 37°C in a water bath and mixed every 15 min by tube inversion. The lung tissues were ground on a 70-μm cell strainer using a 1cc syringe plunger. The cell strainer was rinsed with approximately 20 mL of PBS 1×. The Cell suspension was centrifuged at 600×*g* for 5 min at 4°C and the supernatant was discarded. Red blood cells (RBCs) were lysed by the addition of 1 mL of RBC lysis buffer for 4 min, and the lysis was stopped with cold PBS 1×. Cell suspension was centrifuged at 600×*g* for 5 min at 4°C and the cell pellet was

suspended in PBS 1×. The number of cells was counted using a Moxi cell counter. The cellular concentration was adjusted at 1×10^7 cells/mL using PBS. Flow cytometry staining was performed on 100 µL of the single cell suspension (1×10^6 cells) in U-bottom 96-wells plates. A pooled cell suspension from all experimental conditions was used to perform unstained and fluorescence minus one (FMO) control. The cells were centrifuged (600×*g*, 5 min at 4°C) and the supernatant was discarded. Cells were suspended in 25 µL of Fc Block (BD Biosciences, cat. num. 553142) and incubated for 10 min on ice. The extracellular primary antibodies mix (2×) (25 µL) were added to the wells and incubated for another 20 min on ice in the dark. Both Fc Block and antibody mix were prepared in staining buffer (1% BSA, 0.1% sodium azide). Following incubation, the cells were centrifuged (600×*g*, 5 min at 4°C) and washed twice with staining buffer. For intracellular staining, the cells were suspended in 100 µL of BD fixation/permeabilization solution (BD Bioscience, cat. num. 554714) and incubated for 20 min at 4°C in the dark. The cells were washed once with BD permeabilization buffer (BD Bioscience, cat. num. 554714) and suspended with 50 µL of the intracellular primary antibody solution prepared in this permeabilization buffer. The cells were incubated for 30 min at 4°C in the dark and washed twice with permeabilization buffer. The secondary antibody was added and incubated for 30 min at 4°C in the dark. The cells were washed twice and suspended in FACS Flow (BD Bioscience, cat. num. 336524). The fluorescence spillover was compensated using compensation beads (BD Bioscience, cat. num. 552844). The data were acquired on the BD LSR Fortessa X-20 flow cytometer. The flow cytometry data were analyzed using FlowJo software (BD). The doublets were discriminated using FCS-W/FCS-H and SSC-W/SSC-H and debris were eliminated according to the size (FCS-A) and SSC-A of the recorded events. Leukocytes were identified as $CD45^+$, epithelial cells were identified as $CD45^-CD326^+CD31^-$and club cells were identified as $CD45^-CC10^+$ as summarized in Table S2. Gates for cell population were fixed based on the FMO control (Figure S29). EGFP-positive cells were selected based on baseline fluorescence signal in PBS control mice.

Microscopy imaging

For *in vitro* studies, fluorescence live microscopy images of cells were captured directly on the 96 well plate using a Revolve R4 hybrid inverted fluorescence microscope in the upright position (Echo, BICO company) at 20× magnification. The focus was manually performed, and the fluorescence intensity was adjusted automatically for each well. The Hoechst 33342, $EGFP^+$, and $sCy5^+$ cells were analyzed using the DAPI, fluorescein isothiocyanate, and Cy5 filters, respectively. Supplemental microscopy images are provided for each condition (Figures S21, S25, S32, and S34).

For *in vivo* study, the left lungs were fixed with 4% PFA overnight at 4°C and immersed in a 30% sucrose solution for 24 h at 4°C. Tissues were transferred to a 20% sucrose:OCT (1:1) solution, cut into 7-µm-thick sections with a cryostat, and mounted on glass slides with a coverslip using a Prolong Glass NucBlue (Invitrogen) as an antifading medium. Sections were collected every 300 µm. Slides were incubated overnight in the dark before imaging. Images were taken with an automated slide scanner (PANNORAMIC MIDI II, 3DHistech Ltd.) within 1–4 days after mounting. To increase the sensitivity of the EGFP detection, an immunofluorescence staining was performed. The slides were air-dried and fixed with 4% PFA for 20 min. The tissues were permeabilized with PBS, 0.3% Triton X-100 for 10 min. The tissues were surrounded with a PAP pen and blocked with PBS 5% BSA for 1 h. The antibody rabbit anti-mouse EGFP (Abcam, cat no. Ab6556) was diluted $^1/_2$,500 in the blocking buffer and incubated overnight at 4°C. The slides were washed with PBS (3 × 5 min) and incubated with the secondary antibody donkey anti-rabbit IgG H&L AF594 (Cell Signaling, cat no. A32754) diluted 1/1,000 for 1 h at room temperature. The slides were mounted with Prolong Glass NucBlue. Quantitation of the $sCy5^+$ and $EGFP^+$ cells in the airway epithelium was performed using the CellQuant module and the CaseViewer software from 3DHistech. Supplemental microscopy images are provided for each condition (Figures S28 and S36).

Statistical analysis

Statistical analysis and graphing were performed using Graph Pad Prism. For *in vitro* studies, all represented data for a given assay indicate a minimum experiment replicate of $n = 3$. Statistical significance in the percentage of delivery between conjugates and the control was determined using a two-way ANOVA and Tukey's multiple comparisons tests ($p \leq 0.05$). For *in vivo* studies, statistical significance was determined using a two-way or one-way ANOVA when applicable with Tukey's post hoc test for multiple comparisons ($p \leq 0.05$). The presented data were generated in a single experiment with n = 3–6 per group.

DATA AND CODE AVAILABILITY

Methods for the synthesis of all compounds and characterization by UPLC and MS, cell viability for all *in vitro* assays, additional data for *in vitro* and *in vivo* studies, and UPLC chromatograms related to the GSH-mediated disulfide bond cleavage are presented.

SUPPLEMENTAL INFORMATION

Supplemental information can be found online at https://doi.org/10.1016/j.omtn.2024.102290.

ACKNOWLEDGMENTS

This work is supported by the CQDM (Consortium québécois sur la découverte du médicament) Quantum Leap grant Couture-QL-274. M.A. and L.F.S. acknowledge a financial contribution via the NSERC-CREATE PrEEmiuM program (511957-2018). L.F.G. acknowledges scholarships from the FRQS and NSERC CREATE as part of the RNA innovation program. The authors would like to thank Ms. Vanessa Lapointe and Ms. Isabelle Bolduc for their technical assistance in the conduct of the *in vivo* work and for the histological analyses. F.C. is a member of the Institute of Nutrition and Functional Foods (INAF) of University Laval (Québec, Canada) and of the Research Center of the CISSS de Chaudière-Appalaches (Lévis, Canada).

AUTHOR CONTRIBUTIONS

A.H.S., D.G., and B.G. designed the study; M.A., L.F.S., and N.B. jointly performed experiments and analyzed the *in vitro* results; C.A.H. and F.C. performed and analyzed the *in vivo* results; L.F.G. and I.A. assisted in the *in vitro* experiments and chemical syntheses respectively; M.H. and X.C. generated the modified HeLa cells. The manuscript was written through the contributions of all authors. All authors have reviewed and approved the submission.

DECLARATION OF INTERESTS

D.G. holds equity in Feldan Therapeutics. N.B., M.A., L.S.M., I.A., L.F.G., X.C., M.H., D.G., and A.H.S. are employees of Feldan Therapeutics. A.H.S. and D.G. have filed patent applications. A.H.S. and D.G. are inventors of a patent related to peptide bioconjugates as delivery agent, and D.G. is also inventor of patents related to peptide-based delivery agents, which are assigned to Feldan Bio Inc.

REFERENCES

1. Newman, S.P. (2017). Drug delivery to the lungs: challenges and opportunities. Ther. Deliv. *8*, 647–661. https://doi.org/10.4155/TDE-2017-0037.
2. Liang, W., Pan, H.W., Vllasaliu, D., and Lam, J.K.W. (2020). Pulmonary Delivery of Biological Drugs. Pharmaceutics *12*, 1025–1028. https://doi.org/10.3390/PHARMACEUTICS12111025.
3. Nawroth, J.C., Van Der Does, A.M., Ryan, A., and Kanso, E. (2020). Multiscale mechanics of mucociliary clearance in the lung. Philosophical Transactions of the Royal Society B *375*, 20190160. https://doi.org/10.1098/RSTB.2019.0160.
4. Ma, C.-C., Wang, Z.-L., Xu, T., He, Z.-Y., and Wei, Y.-Q. (2020). The approved gene therapy drugs worldwide: from 1998 to 2019. Biotechnol. Adv. *40*, 107502. https://doi.org/10.1016/j.biotechadv.2019.107502.
5. Shen, X., and Corey, D.R. (2018). Chemistry, mechanism and clinical status of antisense oligonucleotides and duplex RNAs. Nucleic Acids Res. *46*, 1584–1600. https://doi.org/10.1093/NAR/GKX1239.
6. Oren, Y.S., Avizur-Barchad, O., Ozeri-Galai, E., Elgrabli, R., Schirelman, M.R., Blinder, T., Stampfer, C.D., Ordan, M., Laselva, O., Cohen-Cymberknoh, M., et al. (2022). Antisense oligonucleotide splicing modulation as a novel Cystic Fibrosis therapeutic approach for the W1282X nonsense mutation. J. Cyst. Fibros. *21*, 630–636. https://doi.org/10.1016/J.JCF.2021.12.012.
7. Kim, Y.J., Sivetz, N., Layne, J., Voss, D.M., Yang, L., Zhang, Q., and Krainer, A.R. (2022). Exon-skipping antisense oligonucleotides for cystic fibrosis therapy. Proc. Natl. Acad. Sci. USA *119*, e2114858118. https://doi.org/10.1073/PNAS.2114858118/SUPPL_FILE/PNAS.2114858118.SAPP.PDF.
8. Michaels, W.E., Pena-Rasgado, C., Kotaria, R., Bridges, R.J., and Hastings, M.L. (2022). Open reading frame correction using splice-switching antisense oligonucleotides for the treatment of cystic fibrosis. Proc. Natl. Acad. Sci. USA *119*, e2114886119. https://doi.org/10.1073/PNAS.2114886119/SUPPL_FILE/PNAS.2114886119.SAPP.PDF.
9. Ozeri-Galai, E., Friedman, L., Barchad-Avitzur, O., Markovetz, M.R., Boone, W., Rouillard, K.R., Stampfer, C.D., Oren, Y.S., Hill, D.B., Kerem, B., et al. (2023). Delivery Characterization of SPL84 Inhaled Antisense Oligonucleotide Drug for 3849 + 10 kb C- > T Cystic Fibrosis Patients. https://home.liebertpub.com/nat.10.1089/NAT.2023.0015.
10. Popescu, F.-D., and Popescu, F. (2007). A review of antisense therapeutic interventions for molecular biological targets in asthma. Biologics. *1*, 271–283.
11. Boboltz, A., Kumar, S., and Duncan, G.A. (2023). Inhaled drug delivery for the targeted treatment of asthma. Adv. Drug Deliv. Rev. *198*, 114858. https://doi.org/10.1016/J.ADDR.2023.114858.
12. Li, C., Callahan, A.J., Simon, M.D., Totaro, K.A., Mijalis, A.J., Phadke, K.S., Zhang, G., Hartrampf, N., Schissel, C.K., Zhou, M., et al. (2021). Fully automated fast-flow synthesis of antisense phosphorodiamidate morpholino oligomers. Nat. Commun. *12*, 4396–4398. https://doi.org/10.1038/s41467-021-24598-4.
13. Amantana, A., and Iversen, P.L. (2005). Pharmacokinetics and biodistribution of phosphorodiamidate morpholino antisense oligomers. Curr. Opin. Pharmacol. *5*, 550–555. https://doi.org/10.1016/J.COPH.2005.07.001.
14. Iversen, P.L. (2001). Phosphorodiamidate morpholino oligomers: favorable properties for sequence-specific gene inactivation. Curr. Opin. Mol. Therapeut. *3*, 235–238.
15. Stein, C.A., and Castanotto, D. (2017). FDA-Approved Oligonucleotide Therapies in 2017. Mol. Ther. *25*, 1069–1075. https://doi.org/10.1016/j.ymthe.2017.03.023.
16. Lim, K.R.Q., Maruyama, R., and Yokota, T. (2017). Eteplirsen in the treatment of Duchenne muscular dystrophy. Drug Des. Dev. Ther. *11*, 533–545. https://doi.org/10.2147/DDDT.S97635.
17. Miyatake, S., Mizobe, Y., Takizawa, H., Hara, Y., Yokota, T., Takeda, S., and Aoki, Y. (2018). Exon skipping therapy using phosphorodiamidate morpholino oligomers in the mdx52 mouse model of duchenne muscular dystrophy. Methods Mol. Biol. *1687*, 123–141. https://doi.org/10.1007/978-1-4939-7374-3_9/COVER.
18. Anwar, S., and Yokota, T. (2020). Golodirsen for Duchenne muscular dystrophy. Drugs Today *56*, 491–504. https://doi.org/10.1358/DOT.2020.56.8.3159186.
19. Cirak, S., Arechavala-Gomeza, V., Guglieri, M., Feng, L., Torelli, S., Anthony, K., Abbs, S., Garralda, M.E., Bourke, J., Wells, D.J., et al. (2011). Exon skipping and dystrophin restoration in patients with Duchenne muscular dystrophy after systemic phosphorodiamidate morpholino oligomer treatment: An open-label, phase 2, dose-escalation study. Lancet *378*, 595–605. https://doi.org/10.1016/S0140-6736(11)60756-3.
20. Allen, D.G., and Whitehead, N.P. (2011). Duchenne muscular dystrophy – What causes the increased membrane permeability in skeletal muscle? Int. J. Biochem. Cell Biol. *43*, 290–294. https://doi.org/10.1016/j.biocel.2010.11.005.
21. Houang, E.M., Sham, Y.Y., Bates, F.S., and Metzger, J.M. (2018). Muscle membrane integrity in Duchenne muscular dystrophy: recent advances in copolymer-based muscle membrane stabilizers. Skeletal Muscle *8*, 31. https://doi.org/10.1186/s13395-018-0177-7.
22. Iversen, P.L., Aird, K.M., Wu, R., Morse, M.M., and Devi, G.R. (2009). Cellular Uptake of Neutral Phosphorodiamidate Morpholino Oligomers. Curr. Pharm. Biotechnol. *10*, 579–588. https://doi.org/10.2174/138920109789069279.
23. Dang, Y., van Heusden, C., Nickerson, V., Chung, F., Wang, Y., Quinney, N.L., Gentzsch, M., Randell, S.H., Moulton, H.M., Kole, R., et al. (2021). Enhanced delivery of peptide-morpholino oligonucleotides with a small molecule to correct splicing defects in the lung. Nucleic Acids Res. *49*, 6100–6113. https://doi.org/10.1093/nar/gkab488.
24. Juliano, R.L. (2021). Chemical Manipulation of the Endosome Trafficking Machinery: Implications for Oligonucleotide Delivery. Biomedicines *9*, 512. https://doi.org/10.3390/BIOMEDICINES9050512.
25. Juliano, R.L. (2016). The delivery of therapeutic oligonucleotides. Nucleic Acids Res. *44*, 6518–6548. https://doi.org/10.1093/NAR/GKW236.
26. Betts, C., Saleh, A.F., Arzumanov, A.A., Hammond, S.M., Godfrey, C., Coursindel, T., Gait, M.J., and Wood, M.J. (2012). Pip6-PMO, A New Generation of Peptide-oligonucleotide Conjugates With Improved Cardiac Exon Skipping Activity for DMD Treatment. Mol. Ther. Nucleic Acids *1*, e38. https://doi.org/10.1038/mtna.2012.30.
27. Moustafa, D.A., Wu, A.W., Zamora, D., Daly, S.M., Sturge, C.R., Pybus, C., Geller, B.L., Goldberg, J.B., and Greenberg, D.E. (2021). Peptide-Conjugated Phosphorodiamidate Morpholino Oligomers Retain Activity against Multidrug-Resistant Pseudomonas aeruginosa In Vitro and In Vivo. mBio *12*, e02411-20. https://doi.org/10.1128/mBio.02411-20.
28. Sully, E.K., Geller, B.L., Li, L., Moody, C.M., Bailey, S.M., Moore, A.L., Wong, M., Nordmann, P., Daly, S.M., Sturge, C.R., and Greenberg, D.E. (2017). Peptide-conjugated phosphorodiamidate morpholino oligomer (PPMO) restores carbapenem susceptibility to NDM-1-positive pathogens in vitro and in vivo. J. Antimicrob. Chemother. *72*, 782–790. https://doi.org/10.1093/jac/dkw476.
29. Forand, A., Muchir, A., Mougenot, N., Sevoz-Couche, C., Peccate, C., Lemaitre, M., Izabelle, C., Wood, M., Lorain, S., and Piétri-Rouxel, F. (2020). Combined Treatment with Peptide-Conjugated Phosphorodiamidate Morpholino Oligomer-PPMO and AAV-U7 Rescues the Severe DMD Phenotype in Mice. Mol. Ther. Methods Clin. Dev. *17*, 695–708. https://doi.org/10.1016/j.omtm.2020.03.011.
30. Yang, B., Ming, X., Cao, C., Laing, B., Yuan, A., Porter, M.A., Hull-Ryde, E.A., Maddry, J., Suto, M., Janzen, W.P., and Juliano, R.L. (2015). High-throughput

screening identifies small molecules that enhance the pharmacological effects of oligonucleotides. Nucleic Acids Res. *43*, 1987–1996. https://doi.org/10.1093/nar/gkv060.

31. Juliano, R.L., Wang, L., Tavares, F., Brown, E.G., James, L., Ariyarathna, Y., Ming, X., Mao, C., and Suto, M. (2018). Structure–activity relationships and cellular mechanism of action of small molecules that enhance the delivery of oligonucleotides. Nucleic Acids Res. *46*, 1601–1613. https://doi.org/10.1093/nar/gkx1320.

32. Wang, L., Ariyarathna, Y., Ming, X., Yang, B., James, L.I., Kreda, S.M., Porter, M., Janzen, W., and Juliano, R.L. (2017). A Novel Family of Small Molecules that Enhance the Intracellular Delivery and Pharmacological Effectiveness of Antisense and Splice Switching Oligonucleotides. ACS Chem. Biol. *12*, 1999–2007. https://doi.org/10.1021/acschembio.7b00242.

33. Gushchina, L.V., Vetter, T.A., Frair, E.C., Bradley, A.J., Grounds, K.M., Lay, J.W., Huang, N., Suhaiba, A., Schnell, F.J., Hanson, G., et al. (2022). Systemic PPMO-mediated dystrophin expression in the Dup2 mouse model of Duchenne muscular dystrophy. Mol. Ther. Nucleic Acids *30*, 479–492. https://doi.org/10.1016/j.omtn.2022.10.025.

34. Moulton, H.M., and Moulton, J.D. (2010). Morpholinos and their peptide conjugates: Therapeutic promise and challenge for Duchenne muscular dystrophy. Biochim. Biophys. Acta *1798*, 2296–2303. https://doi.org/10.1016/j.bbamem.2010.02.012.

35. Krishnamurthy, S., Wohlford-Lenane, C., Kandimalla, S., Sartre, G., Meyerholz, D.K., Théberge, V., Hallée, S., Duperré, A.-M., Del'Guidice, T., Lepetit-Stoffaes, J.-P., et al. (2019). Engineered amphiphilic peptides enable delivery of proteins and CRISPR-associated nucleases to airway epithelia. Nat. Commun. *10*, 4906. https://doi.org/10.1038/s41467-019-12922-y.

36. Luo, M., Ma, J., Cheng, X., Wu, S., Bartels, D.J., Guay, D., Engelhardt, J.F., and Liu, X. (2023). Genome Editing in Ferret Airway Epithelia Mediated by CRISPR/Nucleases Delivered with Amphiphilic Shuttle Peptides. Hum. Gene Ther. *34*, 705–718. https://doi.org/10.1089/HUM.2023.016. https://home.liebertpub.com/hum.

37. Kulhankova, K., Traore, S., Cheng, X., Benk-Fortin, H., Hallée, S., Hallée, S., Roberge, J., Couture, F., Gross, T., Newby, G., et al. (2023). Shuttle Peptide Delivers Base Editor RNPs to Rhesus Monkey Airway Epithelial. Res. Sq. *14*, 1–16. https://doi.org/10.21203/RS.3.RS-2540755/V1.

38. Lu, J., Wu, T., Zhang, B., Liu, S., Song, W., Qiao, J., and Ruan, H. (2021). Types of nuclear localization signals and mechanisms of protein import into the nucleus. Cell Commun. Signal. *19*, 60. https://doi.org/10.1186/s12964-021-00741-y.

39. Cheng, R., Feng, F., Meng, F., Deng, C., Feijen, J., and Zhong, Z. (2011). Glutathione-responsive nano-vehicles as a promising platform for targeted intracellular drug and gene delivery. J. Contr. Release *152*, 2–12. https://doi.org/10.1016/J.JCONREL.2011.01.030.

40. Karimi, M., Zangabad, P.S., Ghasemi, A., and Hamblin, M.R. (2015). Smart internal stimulus-responsive nanocarriers for drug and gene delivery (Morgan & Claypool Publishers, & Institute of Physics (Great Britain)), pp. 1–113. https://doi.org/10.1088/978-1-6817-4257-1.

41. Oestreicher, J., and Morgan, B. (2019). Glutathione: subcellular distribution and membrane transport. Biochem. Cell. Biol. *97*, 270–289. https://doi.org/10.1139/bcb-2018-0189.

42. Evans, B.J., King, A.T., Katsifis, A., Matesic, L., and Jamie, J.F. (2020). Methods to Enhance the Metabolic Stability of Peptide-Based PET Radiopharmaceuticals. Molecules *25*, 2314. https://doi.org/10.3390/molecules25102314.

43. Doti, N., Mardirossian, M., Sandomenico, A., Ruvo, M., and Caporale, A. (2021). Recent Applications of Retro-Inverso Peptides. Int. J. Mol. Sci. *22*, 8677. https://doi.org/10.3390/ijms22168677.

44. Go, Y.-M., and Jones, D.P. (2008). Redox compartmentalization in eukaryotic cells. Biochim. Biophys. Acta *1780*, 1273–1290. https://doi.org/10.1016/j.bbagen.2008.01.011.

45. Deng, Z., Hu, J., and Liu, S. (2020). Disulfide-Based Self-Immolative Linkers and Functional Bioconjugates for Biological Applications. Macromol. Rapid Commun. *41*, 1900531. https://doi.org/10.1002/marc.201900531.

46. Chen, G., Korfhagen, T.R., Xu, Y., Kitzmiller, J., Wert, S.E., Maeda, Y., Gregorieff, A., Clevers, H., and Whitsett, J.A. (2009). SPDEF is required for mouse pulmonary goblet cell differentiation and regulates a network of genes associated with mucus production. J. Clin. Invest. *119*, 2914–2924. https://doi.org/10.1172/JCI39731.

47. Blyth, D.I., Pedrick, M.S., Savage, T.J., Bright, H., Beesley, J.E., and Sanjar, S. (2012). Induction, Duration, and Resolution of Airway Goblet Cell Hyperplasia in a Murine Model of Atopic Asthma: Effect of Concurrent Infection with Respiratory Syncytial Virus and Response to Dexamethasone. Am. J. Respir. Cell Mol. Biol. *19*, 38–54. https://doi.org/10.1165/ajrcmb.19.1.2930.

48. Vulin, A., Wein, N., Simmons, T.R., Rutherford, A.M., Findlay, A.R., Yurkoski, J.A., Kaminoh, Y., and Flanigan, K.M. (2015). The first exon duplication mouse model of Duchenne muscular dystrophy: A tool for therapeutic development. Neuromuscul. Disord. *25*, 827–834. https://doi.org/10.1016/j.nmd.2015.08.005.

49. Sazani, P., Kang, S.-H., Maier, M.A., Wei, C., Dillman, J., Summerton, J., Manoharan, M., and Kole, R. (2001). Nuclear antisense effects of neutral, anionic and cationic oligonucleotide analogs. Nucleic Acids Res. *29*, 3965–3974. https://doi.org/10.1093/nar/29.19.3965.

50. McClorey, G., and Banerjee, S. (2018). Cell-Penetrating Peptides to Enhance Delivery of Oligonucleotide-Based Therapeutics. Biomedicines *6*, 51. https://doi.org/10.3390/BIOMEDICINES6020051.

51. Abes, S., Turner, J.J., Ivanova, G.D., Owen, D., Williams, D., Arzumanov, A., Clair, P., Gait, M.J., and Lebleu, B. (2007). Efficient splicing correction by PNA conjugation to an R6-Penetratin delivery peptide. Nucleic Acids Res. *35*, 4495–4502. https://doi.org/10.1093/NAR/GKM418.

52. Boisguérin, P., Deshayes, S., Gait, M.J., O'Donovan, L., Godfrey, C., Betts, C.A., Wood, M.J.A., and Lebleu, B. (2015). Delivery of therapeutic oligonucleotides with cell penetrating peptides. Adv. Drug Deliv. Rev. *87*, 52–67. https://doi.org/10.1016/J.ADDR.2015.02.008.

53. Langel, Ü. (2023). Toxicity and Immune Response. In CPP, Cell-Penetrating Peptides, Ü. Langel, ed. (Springer, Cham), pp. 345–357. https://doi.org/10.1007/978-3-031-38731-9_13.

54. Lai, S.H., Stein, D.A., Guerrero-Plata, A., Liao, S.L., Ivanciuc, T., Hong, C., Iversen, P.L., Casola, A., and Garofalo, R.P. (2008). Inhibition of respiratory syncytial virus infections with morpholino oligomers in cell cultures and in mice. Mol. Ther. *16*, 1120–1128. https://doi.org/10.1038/mt.2008.81.

55. Abes, S., Moulton, H.M., Clair, P., Prevot, P., Youngblood, D.S., Wu, R.P., Iversen, P.L., and Lebleu, B. (2006). Vectorization of morpholino oligomers by the (R-Ahx-R)4 peptide allows efficient splicing correction in the absence of endosomolytic agents. J. Contr. Release *116*, 304–313. https://doi.org/10.1016/J.JCONREL.2006.09.011.

56. Vivès, E., Granier, C., Prevot, P., and Lebleu, B. (1997). Structure–activity relationship study of the plasma membrane translocating potential of a short peptide from HIV-1 Tat protein. Lett. Pept. Sci. *4*, 429–436. https://doi.org/10.1023/A:1008850300184.

57. Wan, X., Zhang, J., Yu, W., Shen, L., Ji, S., and Hu, T. (2017). Effect of protein immunogenicity and PEG size and branching on the anti-PEG immune response to PEGylated proteins. Process Biochem. *52*, 183–191. https://doi.org/10.1016/J.PROCBIO.2016.09.029.

58. Vivès, E., Brodin, P., and Lebleu, B. (1997). A Truncated HIV-1 Tat Protein Basic Domain Rapidly Translocates through the Plasma Membrane and Accumulates in the Cell Nucleus. J. Biol. Chem. *272*, 16010–16017. https://doi.org/10.1074/JBC.272.25.16010.

59. Shi, D., Beasock, D., Fessler, A., Szebeni, J., Ljubimova, J.Y., Afonin, K.A., and Dobrovolskaia, M.A. (2022). To PEGylate or not to PEGylate: Immunological properties of nanomedicine's most popular component, polyethylene glycol and its alternatives. Adv. Drug Deliv. Rev. *180*, 114079. https://doi.org/10.1016/J.ADDR.2021.114079.

60. Silhol, M., Tyagi, M., Giacca, M., Lebleu, B., and Vivès, E. (2002). Different mechanisms for cellular internalization of the HIV-1 Tat-derived cell penetrating peptide and recombinant proteins</br>fused to Tat. Eur. J. Biochem. *269*, 494–501. https://doi.org/10.1046/J.0014-2956.2001.02671.X.

61. Khalil, A., Würthwein, G., Golitsch, J., Hempel, G., Fobker, M., Gerss, J., Möricke, A., Zimmermann, M., Smisek, P., Zucchetti, M., et al. (2022). Pre-existing antibodies against polyethylene glycol reduce asparaginase activities on first administration of pegylated E. coli asparaginase in children with acute lymphocytic leukemia. Haematologica *107*, 49–57. https://doi.org/10.3324/HAEMATOL.2020.258525.

62. Stone, C.A., Liu, Y., Relling, M.V., Krantz, M.S., Pratt, A.L., Abreo, A., Hemler, J.A., and Phillips, E.J. (2019). Immediate Hypersensitivity to Polyethylene Glycols and

Polysorbates: More Common Than We Have Recognized. J. Allergy Clin. Immunol. Pract. *7*, 1533–1540.e8. https://doi.org/10.1016/J.JAIP.2018.12.003.

63. Kathiriya, J.J., Brumwell, A.N., Jackson, J.R., Tang, X., and Chapman, H.A. (2020). Distinct Airway Epithelial Stem Cells Hide among Club Cells but Mobilize to Promote Alveolar Regeneration. Cell Stem Cell *26*, 346–358.e4. https://doi.org/10.1016/j.stem.2019.12.014.

64. Tata, P.R., Mou, H., Pardo-Saganta, A., Zhao, R., Prabhu, M., Law, B.M., Vinarsky, V., Cho, J.L., Breton, S., Sahay, A., et al. (2013). Dedifferentiation of committed epithelial cells into stem cells in vivo. Nature *503*, 218–223. https://doi.org/10.1038/nature12777.

65. Rawlins, E.L., Okubo, T., Xue, Y., Brass, D.M., Auten, R.L., Hasegawa, H., Wang, F., and Hogan, B.L.M. (2009). The Role of Scgb1a1+ Clara Cells in the Long-Term Maintenance and Repair of Lung Airway, but Not Alveolar, Epithelium. Cell Stem Cell *4*, 525–534. https://doi.org/10.1016/j.stem.2009.04.002.

66. Greschner, A., Brahiti, N., Auger, M., Hu, L., Soleymani Abyaneh, H., Barbeau, X., Parent, V., Gaillet, B., Guay, D., Soultan, A.-H., et al. (2023). PEGylation of a peptide-based amphiphilic delivery agent and influence on protein delivery to cells. Biomacromolecules *24*, 4890–4900.

67. Rock, J.R., Onaitis, M.W., Rawlins, E.L., Lu, Y., Clark, C.P., Xue, Y., Randell, S.H., and Hogan, B.L.M. (2009). Basal cells as stem cells of the mouse trachea and human airway epithelium. Proc. Natl. Acad. Sci. USA *106*, 12771–12775. https://doi.org/10.1073/PNAS.0906850106/SUPPL_FILE/0906850106SI.PDF.

68. Chen, Y., Toth, R., Chocarro, S., Weichenhan, D., Hey, J., Lutsik, P., Sawall, S., Stathopoulos, G.T., Plass, C., and Sotillo, R. (2022). Club cells employ regeneration mechanisms during lung tumorigenesis. Nat. Commun. *13*, 4557–4616. https://doi.org/10.1038/s41467-022-32052-2.

69. Zhai, J., Emond, M.J., Spangenberg, A., Stern, D.A., Vasquez, M.M., Blue, E.E., Buckingham, K.J., Sherrill, D.L., Halonen, M., Gibson, R.L., et al. (2022). Club cell secretory protein and lung function in children with cystic fibrosis. J. Cyst. Fibros. *21*, 811–820. https://doi.org/10.1016/J.JCF.2022.03.007.

70. Park, S.Y., Hong, J.Y., Lee, S.Y., Lee, S.H., Kim, M.J., Kim, S.Y., Kim, K.W., Shim, H.S., Park, M.S., Lee, C.G., et al. (2021). Club cell-specific role of programmed cell death 5 in pulmonary fibrosis. Nat. Commun. *12*, 2923–3013. https://doi.org/10.1038/s41467-021-23277-8.

71. Laucho-Contreras, M.E., Polverino, F., Gupta, K., Taylor, K.L., Kelly, E., Pinto-Plata, V., Divo, M., Ashfaq, N., Petersen, H., Stripp, B., et al. (2015). Protective role for club cell secretory protein-16 (CC16) in the development of COPD. Eur. Respir. J. *45*, 1544–1556. https://doi.org/10.1183/09031936.00134214.

72. Blackburn, J.B., Li, N.F., Bartlett, N.W., and Richmond, B.W. (2023). An update in club cell biology and its potential relevance to chronic obstructive pulmonary disease. Am. J. Physiol. Lung Cell Mol. Physiol. *324*, L652–L665. https://doi.org/10.1152/AJPLUNG.00192.2022.

73. Chen, S., Kuhn, M., Prettner, K., Yu, F., Yang, T., Bärnighausen, T., Bloom, D.E., and Wang, C. (2023). The global economic burden of chronic obstructive pulmonary disease for 204 countries and territories in 2020–50: a health-augmented macroeconomic modelling study. Lancet Global Health *11*, e1183–e1193. https://doi.org/10.1016/S2214-109X(23)00217-6.

74. Chronic obstructive pulmonary disease (COPD) (2023). https://www.who.int/news-room/fact-sheets/detail/chronic-obstructive-pulmonary-disease-(copd).

75. Sazani, P., Astriab-Fischer, A., and Kole, R. (2003). Effects of base modifications on antisense properties of 2'-O-methoxyethyl and PNA oligonucleotides. Antisense Nucleic Acid Drug Dev. *13*, 119–128. https://doi.org/10.1089/108729003768247583.

76. Sazani, P., Gemignani, F., Kang, S.H., Maier, M.A., Manoharan, M., Persmark, M., Bortner, D., and Kole, R. (2002). Systemically delivered antisense oligomers upregulate gene expression in mouse tissues. Nat. Biotechnol. *20*, 1228–1233. https://doi.org/10.1038/NBT759.